# A crystal-scale record of recharge and mixing at Rabaul Volcano (Papua New Guinea)

Melina Höhn[1*], Margaret E. Hartley[1], John B. Dikaung[2], Ima Itikarai[2], Kila Mulina[2], Steve Saunders[2], Mikhail Sindang[2], Brendan T. McCormick Kilbride[1]

[1]*Department of Earth and Environmental Sciences, University of Manchester, Manchester, M13 9PL, United Kingdom*

[2]*Rabaul Volcano Observatory, P.O. Box 386, Rabaul, East New Britain Province, Papua New Guinea*

*Corresponding author. E-mail: melina1995.hoehn@gmail.com

**This peer-reviewed preprint has been submitted to EarthArXiv. It has completed an initial round of peer review and revision, and is currently under a second round of review at *Journal of Petrology*. If accepted, the final version will be available from the publisher with a DOI.**

# A crystal-scale record of recharge and mixing at Rabaul Volcano (Papua New Guinea)

Melina Höhn[1*], Margaret E. Hartley[1], John B. Dikaung[2], Ima Itikarai[2], Kila Mulina[2], Steve Saunders[2], Mikhail Sindang[2], Brendan T. McCormick Kilbride[1]

[1]*Department of Earth and Environmental Sciences, University of Manchester, Manchester, M13 9PL, United Kingdom*

[2]*Rabaul Volcano Observatory, P.O. Box 386, Rabaul, East New Britain Province, Papua New Guinea*

*Corresponding author. E-mail: melina1995.hoehn@gmail.com

---

## Abstract

Rabaul is a densely populated caldera volcano in Papua New Guinea that last erupted a caldera-forming volume ~1,400 years ago and has produced numerous intra-caldera eruptions since. Its erupted compositions have commonly been attributed to fractional crystallisation, and although mafic enclaves point to a role for mafic recharge and magma mixing, no study has yet used the crystal cargo itself to test this across multiple eruptions, and the depth, connectivity and evolution of the magma storage system remain poorly resolved. We present the first systematic, multi-eruption crystal-cargo and textural study at Rabaul, characterising the 1937, 1994 and 2014 eruption products (with re-examination of 2006) within a single classification scheme and combine this with whole-rock mixing modelling, machine-learning clinopyroxene

thermobarometry and oxybarometry. Two texturally and compositionally distinct types of mineral clot are identified. Mafic mineral clots, of olivine, calcic plagioclase and magnesian clinopyroxene, are fragments of a basaltic crystal mush. Intermediate mineral clots, of more sodic plagioclase, less magnesian clinopyroxene, orthopyroxene and Ti-magnetite, are fragments of a separate, more evolved andesitic–dacitic mush and are described herein for the first time. Mafic-derived crystals within the intermediate clots show that the intermediate mush inherited material from the basaltic mush. The wider crystal cargo records how these mushes interact: mafic crystals transferred into the resident, evolved magma acquired low-anorthite and low-magnesium overgrowth rims, and developed quench-crystallised crystal clusters, olivine-to-orthopyroxene reactions and reverse-zoned recharge bands, all recording mafic recharge and mixing. Our two-endmember mixing model reproduces every post-caldera eruption as a mixture of a resident dacite and a mafic recharge magma. Clinopyroxene thermobarometry yields crystallisation pressures of 200 ± 50 MPa (50–500 MPa) and temperatures of 1050 ± 50 °C (960–1125 °C). Oxybarometry yields ΔQFM ≈ +1, typical of arc magmas. This systematic classification of the crystal cargo across multiple Rabaul eruptions reveals that the volcano is underlain by at least two distinct crystal mushes of basaltic and andesitic–dacitic composition, that exchange crystals and are repeatedly reactivated by mafic recharge, providing a crystal-scale framework for interpreting the compositions and activity of this hazardous caldera.

**Key Words:** magma mixing; magma recharge; magma storage; Rabaul; thermobarometry

# Introduction

Mafic recharge is one of the fundamental processes governing the evolution of arc magmas. When a hotter, more primitive magma intrudes a shallower, cooler, more evolved reservoir, it commonly drives magma mixing (Anderson, 1976; Sparks *et al.,* 1977; Cashman & Sparks, 2013), producing hybrid magmas and much of the compositional diversity erupted at arc volcanoes (Reubi & Blundy, 2009; Ruprecht *et al.,* 2012). Recharge acts not on a simple magma chamber but on a vertically extensive, mush-dominated plumbing system, where interconnected networks of melt-rich zones exist within a crystal-mush framework, distributed across multiple storage levels throughout the crust (Annen *et al.,* 2006; Edmonds *et al.,* 2019; Sparks *et al.,* 2019; Horn *et al.,* 2022), as seismic tomography of many systems has revealed (Delph *et al.,* 2017; Paulatto *et al.,* 2019). How and where mafic magma is injected into such a system, and how recharge melt interacts with the resident crystal mush, therefore exerts a first-order control on the compositions the system erupts and on the assembly and reactivation of its reservoirs (Viccaro *et al.,* 2012; Mangler *et al.,* 2022; Takach *et al.,* 2024).

The most direct archive of recharge and mixing processes is the crystal cargo of the erupted products. Individual crystals nucleate and grow at different times and in different parts of the plumbing system, and record the conditions they experienced in their compositions and zoning. Resorption surfaces, normally and reversely zoned rims, and diffusion-modified boundaries each track changes in temperature, pressure and melt composition, and thus the history of recharge and mixing (Costa *et al.,* 2008; Streck, 2008; Ubide *et al.,* 2021; Morgavi *et al.,* 2022). Crystals may also occur as mineral clots, i.e. coherent aggregates of several phases, which sample fragments of the crystal mush from which they were disaggregated, such that different clot assemblages can fingerprint distinct mush reservoirs (Cashman *et al.,* 2017; Ubide &

Kamber, 2018). Because this record survives at the crystal scale, it can preserve information about the magmas and reservoirs involved even where efficient mixing has homogenised the bulk chemistry of the erupted magma (Davidson *et al.,* 2007). A systematic classification of crystal populations and clot types in a suite of eruptions, and interpretation of their zoning and reaction textures, therefore provides a powerful means of reconstructing how mush-dominated plumbing systems are assembled and reactivated by recharge.

Rabaul Caldera, on the eastern tip of the island of New Britain, Papua New Guinea, is a densely populated and frequently active arc volcano with a long history of caldera-forming eruptions and smaller post-caldera eruptions (Nairn *et al.*, 1995; Wood *et al.*, 1995; Patia, 2004), making the processes that drive its eruptions a matter of direct hazard relevance. Most Rabaul rocks plot along a single linear "main series" trend on Total Alkali vs Silica and other major element diagrams (Wood *et al.*, 1995; Patia, 2004), that has traditionally been interpreted as representing a single liquid line of descent controlled by fractional crystallisation (Heming, 1974; Wood *et al.*, 1995; Patia, 2004). Mafic mineral clots, interpreted as mafic enclaves, are common in Rabaul's erupted products, and previous whole-rock and mass balance studies have shown that basalt-dacite mixing is an important process in the assembly of post-caldera magmas (Bouvet de Maisonneuve *et al.*, 2015; Patia *et al.*, 2017; Fabbro *et al.*, 2020).

Petrological studies of Rabaul have examined the crystal cargo of individual eruptions and modelled mixing from whole-rock arrays or MELTS calculations (Bouvet de Maisonneuve *et al.,* 2015; Patia *et al.,* 2017; Fabbro *et al.,* 2020), but to date, no systematic, consistent characterisation of crystal cargo across multiple post-caldera eruptions has been undertaken. Crystal populations have not been classified within a single petrogenetic scheme, and neither individual crystals nor mineral clots have been distinguished into compositionally and

texturally distinct types that can be linked to specific mush reservoirs. The crystal populations, their zoning and reaction textures, and the mineral clots therefore remain an under-used archive of recharge, mixing and mush remobilisation processes at Rabaul. Independent geophysical imaging provides a broad structural context showing two low-velocity zones beneath the caldera, at 0.5–4 km and 9–18 km depth, interpreted as a shallow evolved reservoir and a deeper zone that may store mafic magmas (Finlayson *et al.,* 2003; Bai & Greenhalgh, 2005; Itikarai, 2008). However, the depth, connectivity and temporal evolution of these storage zones remain uncertain. The crystal-scale petrological record offers an independent means of probing the architecture of this complex system.

We have used the crystal cargo of the 1937, 1994 and 2014 eruptions of Rabaul to reconstruct the magma mixing recorded in these products and the mafic recharge that drove it, and to refine the conceptual architecture of the plumbing system. Moving beyond the established and well-documented paradigm that basalt and dacite mix beneath Rabaul, we provide the first systematic characterisation of the mineral populations and textures that record this process. We identify three plagioclase and two clinopyroxene groups on the basis of their core compositions, zoning and rims, plus two texturally and compositionally distinct types of mineral clot — mafic and intermediate — which we interpret as disaggregated fragments of two separate crystal-mush reservoirs. Zoning and reaction textures, include normal growth zonation, resorption, rapid-growth rims, peritectic replacement of olivine, and reverse-zoned recharge bands. Taken together, these observations allow us to reconstruct the sequence of recharge, crystal transfer and mixing recorded by the cargo. We then place this record in a wider context: we test the inferred mixing relationship with a two-endmember whole-rock model anchored on measured Rabaul compositions, we apply machine-learning clinopyroxene-only and clinopyroxene–liquid thermobarometry for the first time at Rabaul, to assess candidly

what these approaches can and cannot resolve about magma storage depth, and we report the first oxygen-fugacity estimates for Rabaul magmas. Integrating these constraints with the existing geophysical and geochemical record, we develop a refined conceptual model in which Rabaul's magmas are stored in a heterogeneous but interconnected mush dominated plumbing system that is repeatedly reactivated by mafic recharge.

# Geological background

## Tectonic and geographic background

Rabaul is located on the Gazelle Peninsula, northeastern New Britain, positioned within the complex tectonic environment of the converging Pacific and Australian plates (Baldwin *et al.*, 2012; Holm *et al.*, 2016) (Fig. 1a). New Britain is part of the New Britain volcanic arc, which formed in response to the subduction of the Solomon Sea plate beneath the Bismarck Sea plate at the New Britain Trench (Baldwin *et al.*, 2012; Holm *et al.*, 2016).

Rabaul caldera measures 14×9 km and is largely flooded by Blanche Bay (Heming, 1974; Nairn *et al.*, 1995) (Fig. 1b). The caldera formed around 1400 years ago during a major eruption, referred to as the Rabaul Pyroclastics eruption (McKee *et al.*, 2015). The Gazelle Peninsula is densely populated, with the town of Rabaul historically serving as the provincial capital before being heavily damaged by volcanic eruptions, the last time in 1994 (Johnson, 2013). The modern capital Kokopo remains at risk from higher intensity eruptions of Rabaul.

To the northeast of the caldera lie the relatively little-eroded stratovolcanoes Kombiu and Turangunan, and the heavily eroded and breached volcano Palangiangia within which the younger cone of Rabalanakaia has grown (Fig. 1b). These edifices, together with the northern

volcanoes of Tovanumbatir and Watom Island, belong to the Watom-Turangunan-Zone (WTZ), a NW-SE trending zone of predominantly mafic stratovolcanoes (Heming, 1974; McKee & Duncan, 2016). The most active vents within Rabaul caldera in recent history have been Vulcan and Tavurvur, located on the western and eastern sides of Blanche Bay, respectively. These vents have been the source of the most recent explosive eruptions in 1937, 1994, 2006 and 2014 (Heming, 1974; Nairn *et al.*, 1989; Nairn *et al.*, 1995; Patia, 2004).

## Eruption history of Rabaul

Volcanism at Rabaul started >330 kyr ago and includes at least ten dacitic ignimbrite-producing eruptions, some of which were caldera-forming (Nairn *et al.*, 1989; Nairn *et al.*, 1995; Wood *et al.*, 1995; McKee & Duncan, 2016). The Rabaul Pyroclastics eruption, which occurred between 667 and 699 CE (McKee *et al.*, 2015), produced extensive pyroclastic flows and tephra deposits that covered much of the northeastern Gazelle Peninsula. Since this major event, Rabaul has undergone several smaller intra-caldera eruptions of VEI ≤4 (Nairn *et al.*, 1989; Nairn *et al.*, 1995; Wood *et al.*, 1995) (Table 1). This study focuses on eruptive activity since 1937.

In 1937, a twin eruption occurred at both Vulcan and Tavurvur (Patia, 2004). This explosive phreatomagmatic eruption of VEI of 4 (Roggensack *et al.,* 1996; Patia, 2004) ejected ~0.005 $km^3$ of ash and pumice leading to the build-up of a 255 m-high cone that linked the previous Vulcan Island to the mainland. The main phase of activity at both vents ended on 2 June 1937 but isolated vulcanian explosions continued at Tavurvur until 1943 (Patia, 2004).

After four decades of quiescence, Rabaul experienced significant seismic activity and ground deformation in 1983–1985 (McKee *et al.*, 1984; Mori & McKee, 1987). The seismic epicentres

formed a ring pattern tracing the outline of the Rabaul Pyroclastics caldera (Mori & McKee, 1987). These phenomena were interpreted as intrusion of magma beneath the caldera, leading to concerns that an eruption was imminent (Mori & McKee, 1987; Saunders, 2001). However, no eruption occurred.

A further twin eruption of Vulcan and Tavurvur in 1994 was preceded by near-continuous seismic activity of fluctuating intensity (maximum of $M_L$ 5.1) starting on 18 September (Global Volcanism Program, 1994a). Tilt meters recorded uplift of up to 6 m at Vulcan, which resulted in a shift in the southern shoreline to the south by ~70 m (Global Volcanism Program, 1994a). The eruption started on 19 September. Volcanic activity at Vulcan was short-lived and involved a Plinian-style eruption, whereas the volcanic activity at Tavurvur comprised less powerful, but more sustained strombolian activity (Global Volcanism Program, 1994a; Global Volcanism Program, 1994b). The 1994 eruption devastated the town of Rabaul, burying much of the infrastructure under meters of ash and forcing the evacuation of tens of thousands of residents (Global Volcanism Program, 1994a; Johnson, 2013). The twin eruption produced pyroclastic flows, widespread ashfall, and volcanic lightning, disrupting life on the Gazelle Peninsula. Despite the extensive damage, the 1994 eruption resulted in few fatalities, largely due to successful evacuation efforts (Global Volcanism Program, 1994a; Johnson, 2013; Fearnley *et al.*, 2018).

Following the 1994 event, Rabaul entered a phase of intermittent eruptive activity, with periodic explosions, lava dome growth in Tavurvur's crater, and small-to-moderate ash emissions. Discrete, stronger eruptions occurred in 2006 and 2014. The 2006 eruption of Tavurvur started on 7 October and was characterised by ash emissions up to 18 km high, strombolian explosions and lava effusion, but it did not result in significant damage to the

surrounding region. Strombolian activity subsided by the evening of 7 October (Global Volcanism Program, 2006). Mild volcanic activity continued again after November 2006 with periods of weeks to months of quiescence (Global Volcanism Program, 2007; Global Volcanism Program, 2011; Global Volcanism Program, 2013).

The most recent eruption of Tavurvur began on 29 August 2014. Volcanic activity started with a strombolian eruption which included discrete explosions with ejections of volcanic bombs 500–1000 m from the crater, small lava fountains, and an 18 km-high plume with extensive ash fall (Global Volcanism Program, 2014). Volcanic activity lasted ~24 hours with smaller explosions following until 30 August. The release of diffuse, white vapour, was recorded until 2021 (Global Volcanism Program, 2017). Renewed deformation with uplift of up to 39 mm/month and increased seismicity has been detected at Rabaul since September 2021 (Global Volcanism Program, 2021; Saunders *et al.*, 2023). By November 2024, this ongoing uplift has resulted in a cumulative vertical displacement of ~7 cm (Global Volcanism Program, 2024).

The post-1937 eruptions at Rabaul underscore the ongoing volcanic hazards posed by this volcano, and the necessity for continuous monitoring. The persistence of unrest at Tavurvur in particular suggests that Rabaul remains a significant threat to the local population, with the potential for future explosive eruptions. Although many people have resettled from within the caldera to other communities in the region, the risks associated with future eruptions remain high (Johnson, 2013). The Rabaul-Kokopo area remains the economic centre of the East New Britain province and eruptions on the scale of 1994, and certainly of caldera-forming scale, would pose formidable obstacles to growing populations and societal development in the region.

# Analytical methods

## Thin section maps

We analysed one pumice sample from the 1937 eruption, one volcanic bomb and four lava samples from the 1994 eruption, and two volcanic bombs from the 2014 eruption (Table 2). We prepared thin sections from each sample and examined these under a polarising microscope to determine their characteristic mineral assemblage and texture. We conducted petrographic and mineralogical examinations using an FEI Quanta 650 Environmental FEG scanning electron microscope (SEM) at the Department of Earth and Environmental Sciences, University of Manchester, UK. We produced whole-thin-section-maps of representative samples depicting their mineralogy and texture (Supplementary Figs. 1–4). We first acquired back-scattered electron (BSE) and energy-dispersive X-ray (EDX) maps. We processed the EDX data using XMapTools software (Lanari *et al.*, 2023) to produce modal mineralogy maps, which were used to estimate mineral modal abundances and to support the investigation of mineralogy and textural variations within and between samples. Mineral classification was supported by targeted point analyses carried out by electron probe microanalysis (EPMA).

## Whole-rock analysis

For whole-rock analysis, representative sample pieces from each deposit were crushed into <2 mm chips with a stainless steel mortar and then ground into powders using an agate ball mill. Whole-rock compositions were measured by X-ray Fluorescence (XRF) spectroscopy at ETH Zürich, Switzerland. We measured major element oxides $SiO_2$, $TiO_2$, $Al_2O_3$, $Fe_2O_3$, MnO, MgO, CaO, $Na_2O$, $K_2O$, $P_2O5$, $Cr_2O_3$, and NiO. Detailed information on the analytical procedure for XRF analysis can be found in Supplementary File S1. All XRF data can be found in

Supplementary File S2.

## Electron probe microanalysis (EPMA)

We conducted electron microprobe analyses at the Department of Mineralogy, University of Münster, Germany, and the Department of Earth and Environmental Sciences, University of Manchester, UK. We measured core and rim compositions of plagioclase, clinopyroxene, orthopyroxene, and olivine as well as matrix glasses in all of the collected samples from Rabaul. In addition, we measured zoning profiles in plagioclase, clinopyroxene and olivine crystals. Elements analysed were $SiO_2$, $TiO_2$, $Al_2O_3$, $FeO^T$, MnO, MgO, CaO, $Na_2O$, $K_2O$, $P_2O5$, $Cr_2O_3$, and NiO; CoO was included in olivine measurements. We used the optimised analytical set-up of Neave *et al.* (2024) for clinopyroxene analyses to minimise the analytical uncertainty on minor elements and improve precision of thermobarometry calculations (Wieser *et al.,* 2023b; Neave *et al.,* 2024). Matrix glass analyses were screened for possible contamination by adjacent crystals and microlites, and measurements identified as mixed analyses were excluded. We also analysed Ti-magnetite in samples from each Rabaul eruption for oxybarometry. Here, the analysed elements were $SiO_2$, $TiO_2$, $Al_2O_3$, $Fe_2O_3$, FeO, MnO, MgO, CaO, $Na_2O$, $K_2O$, $Cr_2O_3$, NiO, ZnO, and $V_2O_3$. Analytical accuracy and precision were monitored in every session by repeat analyses of mineral and basaltic glass secondary standards. For the major elements measured values were typically reproduced to within ~5% of accepted standard compositions, with relative standard deviations generally ≤2%. Somewhat larger uncertainties apply to FeO, $Na_2O$ and $K_2O$ in feldspars, and to minor and trace elements present near their detection limits in silicate phases (e.g. $TiO_2$, MnO, $P_2O_5$, $Cr_2O_3$, NiO). For the Ti-magnetite analyses used in oxybarometry, FeO and $Fe_2O_3$ were reproduced to within ~2–4% of accepted values. Detailed information on the analytical conditions for EPMA

analysis can be found in Supplementary File S1. All EPMA data can be found in Supplementary Files S3–S7.

## Thermobarometry calculations

We performed clinopyroxene-only and clinopyroxene–liquid thermobarometry calculations using the open-source Python tool Thermobar (Wieser *et al.*, 2022). We applied the machine learning-based models developed by Jorgenson *et al.* (2022) and Petrelli *et al.* (2020), which produce the smallest mismatch between calculated and experimental pressures at the pressure-temperature-melt $H_2O$ conditions relevant to arc settings (Wieser *et al.*, 2023a). All thermobarometry data can be found in Supplementary File S8.

For cpx-liquid thermobarometry, we first performed mineral-melt equilibrium matching. We tested clinopyroxene crystals for equilibrium against a dataset of putative liquid compositions comprising matrix glass and whole-rock analyses based on the following equilibrium conditions. The equilibrium coefficient ($KD_{cpx\text{-}liq}^{Fe\text{-}Mg}$) between clinopyroxene and liquid was set at 0.27 with a 2σ error of 0.08. We considered glass and clinopyroxene to be in equilibrium when the observed DiHd, EnFs and CaTs component values were within ±0.12, ±0.10 and ±0.06 (2 SEE), respectively (Neave *et al.*, 2019). For each equilibrium clinopyroxene-liquid pair, we calculated pressures and temperatures with the Jorgenson *et al.* (2022) and Petrelli *et al.* (2020) models. Pressure-temperature pairs with an interquartile range (IQR) of the voting distribution exceeding 6.8 were discarded, following the recommendation of Jorgenson *et al.* (2022). The same filtering criterion was applied to estimates derived from the Petrelli *et al.* (2020) model, due to the comparable standard error on the pressure. The mean and standard deviation of the pressure–temperature estimates were then determined for each clinopyroxene

crystal. Pressures were subsequently converted to depths using the crustal density model of Rasmussen *et al.* (2022). In parallel, for clinopyroxene-only thermobarometry calculations, we calculated pressures and temperatures with the same models from Jorgenson *et al.* (2022) and Petrelli *et al.* (2020) for each individual clinopyroxene crystal. Afterwards, we applied the IQR >6.8 filter and converted pressures to depth using the crustal density model of Rasmussen *et al.* (2022).

We used a Monte Carlo error propagation implemented in Thermobar to estimate the analytical uncertainty associated with our clinopyroxene-liquid pressure-temperature estimates. We created a set of 20,000 theoretical mineral and melt compositions based on the 1σ analytical clinopyroxene and liquid errors from the EPMA measurements for one matching clinopyroxene and liquid pair for each Rabaul eruption. Afterwards, we calculated pressures and temperatures with the models from Jorgenson *et al*. (2022) and Petrelli *et al.* (2020) for each of the 20,000 matching clinopyroxene and liquid pairs. Supplementary Figure S5 shows the 67% and 95% contours which show the range of pressure-temperature estimates produced by the corresponding fraction of the 20,000 theoretical clinopyroxene-liquid pairs. Analogous Monte Carlo calculations were run for the clinopyroxene-only models (Supplementary Fig. S6). The results show that propagated analytical uncertainty on a single clinopyroxene-liquid equilibrium pair can produce pressure-temperature estimates that vary by 25–100°C and ~0.5 –3 kbar.

## Oxygen fugacity calculations

We used the oxybarometer FETiMM (Arató & Audétat, 2017) to calculate the oxygen fugacity of magmas erupted in 1937, 1994 and 2014 at Rabaul. This oxybarometer uses the partitioning

of Fe and Ti between magnetite and silicate melt to estimate $fO_2$. We analysed 20–32 Ti-magnetite crystals in one volcanic bomb or pumice sample from each eruption (samples 1937_pum_b, S152971a, S153126a, VB_IB02) and calculated the average compositions of the EPMA matrix analyses measured in each sample. The inputs for the oxybarometer are the Fe–Ti exchange coefficient between the magnetite and silicate melt, and the AMCNK component (molar $Al_2O_3/(CaO+Na_2O+K_2O+MgO)$) of the melt compositions.

# Results

## Whole-rock compositions

The sample from the 1937 eruption used in this study is an andesitic pumice, with 62.4 wt% $SiO_2$, 15.4 wt% $Al_2O_3$, 1.7 wt% MgO and 4.3 wt% CaO (blue circles, Fig. 2). This falls within the range of reported compositions of the 1937 eruption (blue diamonds, Fig. 2), whose products span basaltic andesite to dacitic. The two samples with the lowest $SiO_2$ content (49.8 –50.4 wt%) are basaltic enclaves. (Patia, 2004, Patia *et al.*, 2017).

The four lava samples and one volcanic bomb from the 1994 eruption are all andesitic (green circles, Fig. 2), with 58.5–61.4 wt% $SiO_2$, 15.6–16.1 wt% $Al_2O_3$, 2.2–3.2 wt% MgO and 5.1–6.7 wt% CaO. Most other published analyses of the 1994 eruption products indicate more evolved compositions, with $SiO_2$ contents of 60.1 to 65.7 wt% (green diamonds, Fig. 2).

The two volcanic bombs analysed from the 2014 eruption are classified as basaltic andesites (yellow circles, Fig. 2). Sample VB_IA contains 56.3 wt% $SiO_2$, 8.0 wt% CaO, and 4.2 wt% MgO, while sample VB_IB contains 56.9 wt% $SiO_2$, 7.9 wt% CaO, and 4.0 wt% MgO. These compositions place them among the more primitive products from the 2014 event, which range

from basaltic andesite to dacite (yellow diamonds, Fabbro *et al.*, 2020).

## Petrography and mineral assemblage

All samples are grey to dark grey in colour and have porphyritic textures. They contain abundant macrocrysts (defined as crystals isolated in the matrix, 0.5–2 mm in size) as well as glomerocrystic aggregates large enough (0.5–1 cm) to be visible to the naked eye, hereafter referred to as mineral clots. The macrocrysts and mineral clots are embedded in a brown, fine-grained groundmass of microcrystalline plagioclase and clinopyroxene with interstitial glass (Supplementary Figs. S1–S4). The vesicularity of the samples decreases from the pumice (~80 vol%) to the volcanic bombs (~60 vol%) to the lavas (~4–20 vol%).

The bulk mineral assemblage (Table 2) consists of plagioclase, clinopyroxene, orthopyroxene, olivine and Ti-magnetite, with accessory apatite and sulfides (Fig. 3). The principal exception is the pumice from the 1937 Rabaul eruption, which does not contain olivine.

Plagioclase is the most abundant macrocryst phase in every sample (Table 2). Plagioclase macrocrysts are subhedral and range in size from 360×200 μm to 1.4×0.6 mm. Clinopyroxene macrocrysts are typically smaller, subhedral, and measure from 110×220 μm to 330×240 μm. Orthopyroxene and olivine crystals are typically subhedral to euhedral. Ti-magnetite is present as small, subhedral to euhedral crystals dispersed in the matrix, attached to other macrocrysts, and as part of mineral clots.

Mineral clots are glomerocrystic aggregates of multiple grains and can be either mono-mineralic or multi-mineralic. Whole-thin-section scans show that mineral clots and isolated macrocrysts form two separate populations, each making up less than ~10% of the sample area

(Supplementary Figs. S1–S4). The dimensions of mineral clots, and the number and size of the individual crystals within them, vary. In the 2014 volcanic bombs, the smallest observed mineral clot measures 250×300 μm and the largest 5.5×3.8 mm; mineral clots in the 1937, 1994 and 2006 eruption products have similar size ranges.

## Macrocrysts

### Plagioclase

Plagioclase crystals plot on the albite-anorthite axis in the plagioclase classification diagram (Supplementary Fig. S7), with compositional ranges of 8.6–21.2 wt% CaO, 0.2–6.3 wt% $Na_2O$, and 0.0–0.5 wt% $K_2O$. The anorthite content (An = molar $CaO/(CaO+Na_2O+K_2O)$) in plagioclase crystals varies from 60 mol% to 95 mol%.

Plagioclase crystals in the Rabaul eruption products can be divided into three groups based on their texture and mineral chemistry (Fig. 3, 4). Group one plagioclase crystals have cores of $An_{85–95}$ ($\sim An_{92}$ is most common, Figs. 4a, 5a), which are resorbed around the edges, and rims of $An_{<62}$ ($\sim An_{53}$ most common, Figs. 4a–b, a–b). Rims of group one cores sometimes feature faint oscillatory zoning (Fig. 4a). Group two plagioclase crystals show patchy zoning with heavily resorbed cores of $An_{65–84}$ and the same rim compositions as group one (Figs. 4b–c, 5b). Group three plagioclase crystals have core compositions below $An_{62}$ with $\sim An_{53}$ being the most common (Fig. 4). The group three plagioclase cores have the same composition as the group one and group two rims. Group three plagioclase crystals can be unzoned or faintly oscillatory zoned with oscillatory zoned crystals spanning from $\sim An_{45}$ to $\sim An_{55}$ (Fig. 4d, 5c).

The 1937 pumice contains group two and group three plagioclase macrocrysts, while the 1994

and 2014 eruption products contain plagioclase belonging to all three groups (Fig. 4). According to our classification, the 2006 eruption products contain mostly group three and group two plagioclase crystals, only a few group one plagioclase crystals with $An_{>85}$ cores have been reported (Bouvet de Maisonneuve *et al.*, 2015).

**Clinopyroxene**

Clinopyroxene crystals are diopsidic to augitic in composition (Supplementary Fig. S8), with FeO contents ranging from 4.7 to 16.9 wt%, MgO from 7.4 to 17.3 wt%, and CaO from 12.8 to 23.8 wt%. Clinopyroxene Mg numbers (Mg# = molar MgO/(MgO+ FeO)) reveal a bimodal distribution of clinopyroxene compositions in the Rabaul samples which we use, along with the mineral textures, to define two groups (Figs. 3, 6). Group one crystals are predominantly Ca-rich diopsides with core compositions of Mg#76–86, most commonly ~Mg#84. These crystals are normally zoned and have rim compositions of Mg#71–77, most commonly ~Mg#75 (Figs. 6a, 7a). Group two clinopyroxene crystals are predominantly augitic, unzoned, and have core compositions of Mg#71–77, most commonly ~Mg#75 (Fig. 6). Rarely, group two clinopyroxene crystals show reverse zoning with core compositions of ~Mg#75, overgrown by alternating bands of high-Mg clinopyroxene with ~Mg#84 and low-Mg clinopyroxene with ~Mg#75 (Fig. 6c–d, 7b). The high-Mg bands in reversely zoned clinopyroxene crystals have markedly higher $Cr_2O_3$ concentrations (0.12–0.24 wt%; mean 0.165 wt%, n = 5) than the adjacent low-Mg bands (≤0.028 wt%; mean 0.009 wt%, n = 8), across all five reverse-zoned crystals identified in the 1994 and 2014 eruption products (Supplementary Table S9, Supplementary Fig. S9).

The 1937 pumice only contains group two clinopyroxene macrocrysts, while the 1994, 2006 and 2014 samples contain both groups of clinopyroxene (Fig. 6) (Bouvet de Maisonneuve *et*

*al.*, 2015).

**Orthopyroxene**

All the analysed samples carry orthopyroxene, and these crystals show uniform textures and compositions across all our samples (Supplementary Fig. S10). They are typically subhedral to euhedral and generally lack zoning, though some orthopyroxene crystals feature thin, Mg-poor rims (Supplementary Fig. S10). Orthopyroxene contains 16.2–18.3 wt% FeO, 22.5–26.0 wt% MgO, 1.3–3.0 wt% CaO, and 0.5–1.9 wt% $Al_2O_3$.

**Olivine**

No olivine was found in the 1937 pumice. Even though olivine was stated to be present in the 2006 eruption products with forsterite (Fo) contents of 69–72 mol% (Fo = molar MgO/(MgO+FeO)) (Bouvet de Maisonneuve *et al.*, 2015), no olivine chemical data were reported for the 2006 eruption products. Olivine crystals in the 1994 and 2014 eruption products are typically subhedral, unzoned and show low-Mg rims (Figs. 3, 8a–b, 9). The modal core composition of olivine crystals is ~$Fo_{80}$ in the 2014 eruption products and ~$Fo_{83}$ in the 1994 products (Fig. 8). The Mg-poor rims around olivine crystals in the 1994 and 2014 samples have compositions of ~$Fo_{65–75}$. Around half of the olivine crystals show variable replacement by orthopyroxene (Fig. 8c–d).

**Ti-magnetite**

The Ti-magnetite crystals have 43.9–48.4 wt% $Fe_2O_3$, 35.0–37.7 wt% FeO, and 9.6–11.6 wt% $TiO_2$. The composition of Ti-magnetite varies slightly between the different eruptions (Fig. 10). The magnetite $FeO^T$ (total iron expressed as FeO) content decreases from an average of 78.4 wt% in the 1937 eruption to an average of 77.9 wt% in the 1994 eruption to an average of

77.4 wt% in the 2014 eruption. In contrast, the $TiO_2$ and $V_2O_3$ concentrations in the magnetite increase over time, from the 1937 (~9.7 wt% $TiO_2$ and ~0.43 wt% $V_2O_3$) to the 1994 (~10.5 wt% $TiO_2$ and ~0.48 wt% $V_2O_3$) to the 2014 eruption (~9.7 wt% $TiO_2$ and ~0.43 wt% $V_2O_3$). The $Al_2O_3$ and MgO concentrations in Ti-magnetite are similar across eruptions within analytical uncertainties (Fig. 10).

## Mineral clots

The plagioclase, clinopyroxene, olivine and orthopyroxene crystals within the mineral clots belong to the same compositional groups, and show the same zoning patterns and resorption textures, as the macrocrysts described above. We therefore use the same group nomenclature throughout.

We distinguish two different types of mineral clots, which we hereafter term ‘mafic’ and ‘intermediate’. Mafic mineral clots consist of variable proportions of group one plagioclase, group one clinopyroxene, olivine and/or minor Ti-magnetite (Figs. 11a–b). Plagioclase is the most abundant phase followed by clinopyroxene, then olivine. Within the mafic mineral clots, grain boundaries between adjacent crystals do not carry the low-An, low-Mg#, and low-Fo rims seen on isolated macrocrysts; these rims occur only on the outer margins of the clots, where crystals are in contact with the matrix glass (Fig. 11a). Mafic mineral clots are typically surrounded by small crystals of olivine (~10×30 μm to ~25×25 μm), Ca-rich clinopyroxene (~25×25 μm to ~25×92 μm), and An-rich plagioclase (~10×50 μm to ~15×150 μm) which stand out from the finer-grained crystals and interstitial glass of the matrix. These clusters of small olivine-cpx-plagioclase crystals are also found in some spots not directly associated with mafic mineral clots (Fig. 11c).

Intermediate mineral clots consist of variable proportions of group two plagioclase, group three plagioclase, group two clinopyroxene, orthopyroxene, and/or Ti-magnetite (Fig. 11d–f). Plagioclase is the most abundant phase, followed by clinopyroxene, then orthopyroxene. The intermediate mineral clots are not surrounded by olivine-clinopyroxene-plagioclase clusters. The group two plagioclase crystals within the intermediate mineral clots are rimmed on all sides by low-An plagioclase (of group three composition), rather than only on their outer margins (Fig. 11e). Although group two clinopyroxene macrocrysts occasionally show reverse zoning, with the high-Mg, high-$Cr_2O_3$ bands described above, no reverse-zoned clinopyroxene was observed within the intermediate mineral clots. In two intermediate mineral clots, orthopyroxene crystals contain small olivine cores surrounded by oxides resembling exsolution lamellae (Fig. 11f).

Both types of mineral clots are found in the 1994 and 2014 eruption products, whereas the 1937 pumice only contains intermediate mineral clots. In the 1994 eruption products, mafic mineral clots account for ~4–26% of the classified clots (~4% in S153127b, ~8% in S152971a, ~10% in S152972, ~20% in S152973, and ~26% in S153126a), with intermediate clots making up the remainder. In the 2014 volcanic bomb (VB_IB02), the proportion of mafic mineral clots is higher, at ~31%. The proportion of mafic mineral clots broadly tracks the bulk composition of the samples, increasing from the more evolved 1994 lavas towards the more mafic 2014 basaltic andesite bombs. Bouvet de Maisonneuve *et al*. (2015) reported the presence of mineral clots in the 2006 eruption products, but their study did not distinguish between different types of mineral clots and not enough textural and chemical information is reported to classify them retrospectively. However, both olivine and orthopyroxene are described as being present in mineral clots from the 2006 eruption products (Bouvet de Maisonneuve *et al.*, 2015). Since our

study shows that olivine only occurs in mafic mineral clots and orthopyroxene only occurs in intermediate mineral clots, we can infer that both mafic and intermediate mineral clots are present in the 2006 eruption products.

## Matrix glass

The matrix glass in the 1937 pumice has 66.5–67.5 wt% $SiO_2$, 15.1–15.6 wt% $Al_2O_3$, 4.3–4.9 wt%, 1.1–1.5 wt% MgO and 3.3–3.7 wt% CaO (blue diamonds, Fig. 12). These dacitic compositions overlap with the 2006 and some of the 1994 matrix glasses.

Matrix glasses in the 1994 eruption products range from dacites to rhyolites, with $SiO_2$ contents of 64.6–78.7 wt% (green circles, Fig. 12, Supplementary Fig. S11). These glasses contain 10.8–16.0 wt% $Al_2O_3$, 0.9–7.1 wt% FeO, up to 4.1 wt% MgO and 0.3–4.5 wt% CaO. Within the 1994 products, the matrix glasses define a continuous evolutionary trend: the least evolved glasses occur in the volcanic bomb S152971 ($SiO_2$ ~64–67 wt%), with compositions overlapping those of the 1937 and 2006 glasses. The glasses become progressively more evolved, lower in MgO, FeO, CaO and $TiO_2$ and higher in $SiO_2$, through the lava S153127 to the most evolved lavas S152972 and S153126, which extend to rhyolitic compositions (up to ~79 wt% $SiO_2$; Supplementary Fig. S12). This trend is consistent with the more extensive groundmass crystallisation expected in the slowly cooled lavas relative to the rapidly quenched bomb.

Matrix glasses in the 2006 samples are andesitic to dacitic, with $SiO_2$ contents between 57.4 and 66.9 wt%. The 2006 matrix glasses record $Al_2O_3$ contents between 13.7 and 15.5 wt%, FeO of 4.4–10.9 wt%, and CaO between 3.1 and 6.6 wt%. The MgO contents in these glasses

are between 1.1 wt% and 3.2 wt% (Bouvet de Maisonneuve *et al.*, 2015).

Matrix glasses in the 2014 volcanic bombs are andesitic with $SiO_2$ of 59.4–65.3 wt% and a comparatively larger range in MgO between 1.3–5.0 wt%. The matrix glasses of the 2014 volcanic bombs vary in $Al_2O_3$ between 12.8 and 16.2 wt%, with FeO from 5.5–8.7 wt% and CaO between 4.2 and 6.9 wt% (Fig. 12, Supplementary Fig. S11).

We tested for equilibrium between minerals and matrix glasses using the $K_D$ values from Putirka (2008) ($K_D(Fe–Mg)^{Ol–liq}$ in the range of 0.30 ±0.03; $K_D(Fe–Mg)^{Cpx–liq}$ in the range of 0.28 ±0.08; $K_D(An\text{-}Ab)^{Pl–liq}$ in the range of 0.27 ±0.11). The matrix glasses span a wide range in Mg# (Fig. 12). Glasses with Mg#30–45 are in equilibrium with group three plagioclase and group two clinopyroxene cores, and with the low-Mg, low-An, and low-Mg# rims around olivine, group one plagioclase, and group one clinopyroxene (Supplementary Figs. S13–S20). This intermediate-Mg# population comprises all of the 1937 matrix glasses and a large proportion of the 2014 matrix glasses, together with a small subset of the 1994 matrix glasses (Fig. 12). The majority of the 1994 matrix glasses, however, are considerably more evolved (Mg# <30, extending below Mg# 20) and are not in equilibrium with any of the analysed crystals. The mafic crystals, $Fo_{>70}$ olivine, group one clinopyroxene (Mg#>77), and group one and group two plagioclase cores ($An_{>65}$), are likewise not in equilibrium with the intermediate-Mg# glasses, and are in equilibrium only with a small subset of glasses with Mg#>45 that occur exclusively within ~50 μm of mafic macrocrysts and mafic mineral clots (Supplementary Figs. S13–S20).

## Thermobarometry

We conducted clinopyroxene-only and clinopyroxene-liquid thermobarometry calculations using the models of Jorgenson *et al.* (2022) and Petrelli *et al.* (2020) to estimate pressures and temperatures of clinopyroxene crystallisation. Clinopyroxene-liquid calculations yield crystallisation pressures between 50 and 450 MPa and temperatures between 960 and 1125 °C (Fig. 13). Clinopyroxene-only calculations yield similar temperatures. The output pressures extend up to 600 MPa, but most of the outputs lie between 50 and 500 MPa with only a few clinopyroxene crystals in the 2014 eruptions products showing higher pressures (Fig. 14). Our calculations suggest no significant difference in the crystallisation pressures and temperatures of clinopyroxene cores and clinopyroxene rims (Supplementary Figs. S23–26).

Using the Jorgenson *et al.* (2022) clinopyroxene-liquid model, mean pressures cluster around 200 ± 50 MPa (Supplementary Fig. S27). Although there is minor scatter between eruptions and between group one and group two crystals, these variations remain within one standard deviation (1σ) and do not reveal any systematic trend. Clinopyroxene-only pressures computed with the same model exhibit greater dispersion: group two crystals from the 1937 eruption and group one crystals from the 1994 and 2014 eruptions average 200 ± 70 MPa, whereas group two crystals from 1994 and 2014 average 170 ± 50 MPa. The mean pressure difference between the two clinopyroxene groups (~30 MPa) is well within 1σ uncertainty. The Petrelli *et al.* (2020) models produce pressures that are ~20 MPa higher than those calculated with the Jorgenson *et al.* (2022) models.

For group one clinopyroxene, Jorgenson *et al.* (2022) clinopyroxene-liquid temperatures average 1057 ± 28°C (1994) and 1067 ± 29°C (2014), while clinopyroxene-only temperatures average 1072 ± 23°C (1994) and 1060 ± 18°C (2014). Petrelli *et al.* (2020) yields temperatures

within 3°C of these values (Fig. 14). For group two clinopyroxene, the Jorgenson model returns clinopyroxene-average liquid temperatures of 995 ± 6°C (1937), 1045 ± 6°C (1994), and 1056 ± 18°C (2014); clinopyroxene-only temperatures are 1035 ± 14°C, 1045 ± 18°C, and 1055 ± 18°C for the same eruptions. Petrelli *et al.* (2020) produces temperature estimates 9–23°C lower than Jorgenson *et al.* (2022) for group two clinopyroxene, except for the 1937 eruption, where the clinopyroxene-liquid result is 21°C higher. Group one clinopyroxene temperatures are consistently slightly higher than those of group two, but this temperature difference also falls within 1σ.

In summary, clinopyroxene crystallisation in the 1937, 1994 and 2014 Rabaul eruption products occurred at pressures of ~200 ± 50 MPa (range 50–500 MPa) and temperatures of ~1050 ± 50°C (range 960–1125°C). The calculated pressure and temperature do not resolve a statistically significant difference in crystallisation conditions between the two clinopyroxene groups, although the slightly higher temperatures of group one are consistent with independent textural and compositional evidence for its derivation from a more mafic reservoir. Fabbro *et al.* (2020) estimated magma storage conditions for the 2014 eruption products to be between 970–1020°C and 40–400 MPa using the two-pyroxene, clinopyroxene-liquid and plagioclase-liquid thermometers and barometers of Putirka (2008). Our P-T results are broadly consistent with these previous estimates. However, Wieser *et al.* (2022) demonstrated that the Putirka (2008) clinopyroxene-liquid barometer underestimates crystallisation pressures for those clinopyroxene crystals in hydrous arc magmas that crystallised deeper than 300 MPa, which could explain the offset with our calculated clinopyroxene pressures of up to 100 MPa. Notably, the Jorgenson *et al.* (2022) model does not incorporate a water term in the liquid component, thereby reducing one source of uncertainty relative to the Putirka (2008) approach, which requires an explicit water input.

### Oxygen fugacity

Our calculations using the FeTIMM oxybarometer (Arató & Audétat, 2017) yield oxygen fugacity conditions of ΔQFM = +1.3 ±0.02 for the 1937 pumice, ΔQFM = +1.1 ±0.2 for the 1994 volcanic bombs, and ΔQFM = +0.9 ±0.1 for the 2014 volcanic bombs. The uncertainties calculated for individual eruptions are comparable with the oxybarometer uncertainty of ±0.2 –0.3 log units $fO_2$ at ≤QFM+1.5.

## Discussion

### Magma storage conditions

Our thermobarometry calculations indicate that group one clinopyroxene records marginally higher pressures (~30 MPa) than group two clinopyroxene (Figs. 13, 14), corresponding to a depth offset of approximately 1.2 km. However, the uncertainties on the thermobarometry models are 320 MPa and 72.5°C for the clinopyroxene-only and 270 MPa and 44.9°C for the clinopyroxene-liquid models of Jorgenson *et al.* (2022), and 300 MPa and 40°C for clinopyroxene-only and 260 MPa and 40°C for the clinopyroxene-liquid models of Petrelli *et al.* (2020). These uncertainties are equivalent to a vertical resolution of ~10–13 km. In fact, Wieser *et al.* (2023a) showed that all commonly used thermobarometers can only distinguish magma storage zones that are at least 10–15 km apart. The absolute depths of clinopyroxene crystallisation beneath Rabaul are therefore poorly constrained, and the ~30 MPa offset between the two groups is well within uncertainty.

Because both clinopyroxene groups were analysed and modelled in an identical manner, the

relative comparison between them is more robust than either absolute estimate. The two groups return essentially indistinguishable mean pressures; had group one and group two crystallised in reservoirs separated by 100–200 MPa, we might expect this to be expressed as a systematic relative offset between the two populations, which we do not observe. Our data are therefore consistent with a mush system in which chemically distinct mafic (group one) and more evolved, intermediate (group two) domains coexist across a common pressure range, such that relative thermobarometry does not resolve a depth separation between them.

Independent constraints on the depth structure of the plumbing system beneath Rabaul are provided by seismic tomography, which has identified two distinct low-velocity zones beneath Rabaul — one at ~0.5–4 km (~10–110 MPa) and the other at ~9–18 km (~234–480 MPa) — interpreted as vertically stacked magma storage regions linked by a low-velocity conduit (Finlayson *et al.,* 2003; Bai & Greenhalgh, 2005; Itikarai, 2008). If the mafic and evolved domains were vertically stratified, these zones might correspond to a deeper, more mafic and a shallower, more evolved magma reservoir. Our thermobarometry can neither confirm nor exclude this configuration: the indistinguishable pressures of the two clinopyroxene groups are equally consistent with the two domains being interleaved at broadly similar crustal levels, or with crystallisation occurring over a wide range of crustal conditions potentially over much of the crustal interval, including storage at ~5–10 km in small lenses that are not resolved by geophysical imaging. Distinguishing between these possibilities is beyond the resolution of the current data. Future work is needed to reduce the uncertainties on thermobarometry calculations, and advances in geophysical imaging may also provide further insights into cryptic magma storage in the arc crust. Although our thermobarometry results do not fully resolve Rabaul's magma plumbing system architecture given current modelling uncertainties, the mineral chemistries and textures of the erupted crystal cargo preserve clear records of

Rabaul's pre-eruptive magma dynamics.

## Magmatic processes recorded by the crystal cargo

### A basaltic mush recorded by the mafic mineral clots

In our mafic mineral clots, the cores of olivine, group one clinopyroxene and group one plagioclase crystals are out of equilibrium with most of our matrix glasses. This indicates that these mafic crystal cores did not grow in the magma in which they were erupted but rather represent a crystal cargo inherited from another source, presumably a magma of lower $SiO_2$ and higher MgO content. We interpret the mafic mineral clots as fragments of basaltic crystal mush that preserve the textural and chemical signature of their source environment. The mafic mineral clots described here correspond to the mafic enclaves and crystal aggregates documented in previous studies of Rabaul, which reported their compositions and, in several cases, their textures (Bouvet de Maisonneuve *et al.,* 2015; Patia *et al.,* 2017; Fabbro *et al.,* 2020). The magnesian clinopyroxene (Mg#81–87), calcic plagioclase ($An_{85–97}$) and olivine ($Fo_{73–86}$) reported for these enclaves and aggregates overlap with our group one plagioclase, group one clinopyroxene and olivine compositions.

Crystals in the mafic mineral clots and mafic macrocrysts exhibit identical mineral chemistries and zoning patterns, pointing to a common origin. The clots are intergrown, cumulate-like aggregates of plagioclase, clinopyroxene and olivine, with resorbed and interstitial grain relationships rather than crystals joined along matching euhedral faces. This texture is more consistent with the crystallisation of these phases together within a crystal mush by in situ growth and heterogeneous nucleation in a liquid-rich, crystal-bearing environment (Hammer *et al.,* 2010; Holness *et al.,* 2023) than with synneusis, the drifting together and face-to-face

attachment of separately grown crystals, which typically produces crystallographically aligned aggregates (Vance, 1969; Schwindinger & Anderson, 1989; Wieser *et al.,* 2019). *In situ* crystallisation is also the mechanism increasingly favoured for the construction of mafic crystal mushes generally, over the gravitational settling of individual crystals, because slowly cooled basaltic reservoirs rarely reach the degree of undercooling required to nucleate crystals within the melt itself (Campbell, 1978; Jaupart & Tait, 1995; Hepworth e*t al.,* 2018; Kruger & Latypov 2020). Settling of individual crystals is in any case an unlikely way to assemble our clots, since plagioclase, clinopyroxene and olivine differ in density and would tend to be sorted rather than concentrated together. Where settling contributes to mush growth, it more plausibly involves dense, pre-formed crystal aggregates. This growing mush was subsequently remobilised, e.g. by melt injection, resulting in partial disaggregation that produced the mafic mineral clots, or wholesale disaggregation that yielded individual mafic macrocrysts, both of which were carried to shallower levels in the plumbing system and erupted (Lissenberg *et al.,* 2019).

**Magma mixing and crystal transfer**

The mafic mineral clots and mafic macrocrysts did not grow in the more evolved magma in which they were erupted, but were introduced during mafic recharge and magma mixing. Mixing between basaltic and dacitic magmas has long been recognised as a dominant control on the compositions of Rabaul's post-caldera eruptives on the basis of whole-rock and glass compositional trends (Bouvet de Maisonneuve *et al.,* 2015; Patia *et al.,* 2017; Fabbro *et al.,* 2020). Here we show that this mixing is also recorded directly in the crystal cargo. Two features record this: crystal cores are out of equilibrium with the resident melt, and they carry low-An, low-Mg# and low-Fo overgrowth rims. We infer that the mafic magma was stored at greater depth than the resident, more evolved magma. This inference does not come from our thermobarometry, which cannot resolve the relative depths of the two magmas, but follows

instead from the deeper of the two seismic low-velocity zones beneath Rabaul (Bai & Greenhalgh, 2005; Itikarai, 2008) and from the general observation that more mafic, primitive magmas are typically sourced from greater depths in vertically extensive, transcrustal magma systems (e.g., Cashman *et al.*, 2017; Edmonds *et al.*, 2019; Sparks *et al.*, 2019). Similar transfer of a mafic crystal cargo into a more evolved magma is documented at other volcanic systems, including Soufrière Hills volcano and Volcán Quizapu in Chile (Humphreys *et al.*, 2009; Ruprecht *et al.,* 2012; Plail *et al.*, 2014; Ubide *et al.*, 2014).

The clearest record of this crystal transfer is the crystal rims. The low-An, low-Mg#, and low-Fo rims around the group one, group one clinopyroxene and olivine cores (Figs. 4, 6, 8) are in equilibrium with the matrix glasses that have Mg#30–45 and with whole-rock compositions (Supplementary Figs. S13–S22). The transition from cores to rims is marked by an abrupt decrease in anorthite content in plagioclase (Fig. 5a) and in Mg# in clinopyroxene (Fig. 7a), with no intermediate compositions. This discrete compositional shift is inconsistent with continuous fractional crystallisation and instead reflects a sudden change in crystallisation conditions (Namur *et al.*, 2020), which could result either from mixing with a more evolved melt or from degassing during ascent.

In plagioclase, both processes can produce an abrupt decrease in anorthite content: mixing lowers the An content of the melt in equilibrium with the rim, while $H_2O$ loss during degassing raises the plagioclase liquidus and likewise favours lower-An crystallisation (Frey & Lange, 2011). Plagioclase zoning alone therefore cannot distinguish between the two mechanisms. The ferromagnesian phases, however, can. The clinopyroxene and olivine rims are distinctly normal-zoned, with sharply lower Mg# and Fo than their cores, as expected for crystallisation from a cooler, more evolved magma following mixing. Degassing would not lower the melt

Mg# in the same way, and would more plausibly produce reverse or weak zoning in these phases (Frey & Lange, 2011; Waters & Lange, 2017). The combination of low-An plagioclase rims with low-Mg# clinopyroxene and low-Fo olivine rims, all in equilibrium with the same evolved matrix glasses, is therefore consistent with mixing and inconsistent with a degassing origin. Comparable rim characteristics have been documented in other volcanic systems undergoing mafic recharge and magma mixing (Coote & Shane, 2016; Namur *et al.*, 2020; Palummo *et al.*, 2021). We therefore interpret these low-An, low-Mg#, and low-Fo rims as overgrowths that formed in equilibrium with a more evolved magma following mixing.

A second textural record of the transfer is the clusters of small (tens of μm) olivine, clinopyroxene and plagioclase crystals that rim the mafic mineral clots and some mafic macrocrysts (Fig. 11a–c). The plagioclase in these clusters occurs as small, elongate to acicular laths with high aspect ratios, and the clusters combine a high crystal number density with small crystal size, in marked contrast to the large, blocky macrocrysts. These features are diagnostic of crystallisation under high undercooling (ΔT), as occurs when a hot mafic magma is intruded into a cooler, more evolved resident magma (Ruprecht *et al.,* 2020). Small crystals of this kind in the 2006 Rabaul eruption products are mafic in composition (Bouvet de Maisonneuve *et al.,* 2015), and in our samples the highest Mg# matrix glasses (>45) occur only within ~50 μm of mafic clots and macrocrysts, showing that a mafic melt envelope surrounded these crystals.

These observations indicate that the small-crystal clusters crystallised rapidly from this mafic melt as it was chilled by the cooler resident magma. As seen in BSE images (Fig. 11a–b), this marginal zone of small crystals forms an open, loosely packed framework rather than a continuous, sealing rind, so that the evolved resident melt was still able to reach the outer surfaces of the clot crystals. This permitted the overgrowth of thin low-An, low-Mg# and low-

Fo rims on the outer clot crystals, while the tightly interlocking clot interiors remained shielded and unrimmed (Fig. 11a–b). Similar clusters of small mafic crystals also occur in areas away from mafic clots (Fig. 11c), consistent with small parcels of mafic melt having been dispersed through the resident magma during mixing.

A third record of crystal transfer is the reaction of olivine to orthopyroxene. Around half of the olivine macrocrysts are partly replaced by orthopyroxene (Fig. 8c–d). Olivine is unstable in contact with silica-rich melt: on entering a more evolved, higher-$SiO_2$ magma, it reacts with silica in the surrounding melt through a peritectic reaction, such that olivine crystals are resorbed and rimmed or replaced by orthopyroxene as they re-equilibrates with the more evolved liquid (Tsuchiyama, 1986). This texture preserves a record of the transfer of olivine crystals from the mafic magma in which they grew into a more silica-rich resident melt during mafic recharge and magma mixing (Coombs & Gardner, 2004; Humphreys *et al.,* 2006; Zellmer *et al.,* 2016).

Plagioclase macrocrysts record the same transfer through their variable resorption. Group one and group two plagioclase crystals share the same low-An ($An_{<62}$) rims, and the cores of both groups are in equilibrium only with the most mafic matrix glasses (Mg#>45). Both groups therefore originated in the mafic magma reservoir and acquired their low-An rims upon mixing with the more evolved melt. They differ only in the degree of core resorption: group two crystals have strongly resorbed, sometimes patchily zoned cores of $An_{65–84}$ (Fig. 4b–c), whereas group one crystals have less resorbed cores of $An_{85–95}$ (Fig. 4a). We interpret this as a single plagioclase population in which individual crystals were resorbed to differing degrees, rather than as two distinct crystal populations. Under this interpretation, the lower An contents of group two crystal cores result from more extensive resorption and dissolution–re-precipitation

(Streck, 2008) rather than a distinct origin, and the apparent degree of resorption also depends on the plane of section, since a more obliquely sectioned or more deeply resorbed crystal exposes more of its lower-An interior. Consistent with this, group one crystals themselves commonly show resorption, including melt inclusions and faint sieve-textured zones (Fig. 4a), and the two groups form overlapping shoulders of a continuous An distribution (Fig. 4) rather than two discrete populations.

How far each crystal was resorbed reflects its exposure to, and residence within, the more evolved melt, and may additionally reflect decompression-induced dissolution during ascent (Streck, 2008; Viccaro *et al.*, 2012; Coote & Shane, 2016; Ubide & Kamber, 2018). Isolated macrocrysts span the full range from group one to group two because each was exposed to the evolved melt for a differing length of time: crystals transferred late, or resident only briefly, retain little-resorbed group one cores, whereas those with longer residence times became progressively more resorbed group two cores. The two clot types mark the extremes of this exposure. Mafic mineral clots preserve unresorbed group one plagioclase crystals because their tightly interlocking interiors were shielded from the evolved melt that percolated through the permeable clot margins, and resorption and low-An rims developed only on the outer margins of the clot where crystals contacted the matrix glass. Intermediate mineral clots, by contrast, contain group two plagioclase crystals that were resorbed and fully rimmed while isolated in the evolved mush before they aggregated into clots.

**An andesitic-dacitic mush recorded by the intermediate mineral clots**

Intermediate mineral clots contain group two plagioclase, group three plagioclase ($An_{<62}$), group two clinopyroxene (Mg#~75), orthopyroxene and Ti-magnetite. The cores of group three plagioclase match the rims of both group one and group two plagioclase. Similarly, the cores

of group two clinopyroxene match the low-Mg# rims around group one clinopyroxene. Both group three plagioclase crystals and group two clinopyroxene crystals are in equilibrium with matrix glasses of Mg#30–45 and with the whole-rock compositions. These phases therefore crystallised *in situ* from the more evolved resident magma, in the same way as the low-An, low-Mg# rims on the group one minerals.

The group two plagioclase crystals in the intermediate clots have a different origin. Their strongly resorbed cores are in equilibrium only with the most mafic matrix glasses (Mg#>45) and are therefore inherited from the mafic magma, whereas their thick rims match the group three plagioclase composition and grew from the evolved resident melt. The group two plagioclase crystals thus record both environments: mafic-derived cores, resorbed and then overgrown by rims that crystallised from the evolved magma. Two of the intermediate clots reinforce this, containing orthopyroxene crystals that enclosed relict olivine cores (Fig. 11f), representing mafic olivine that was entrained into the evolved magma and reacted to orthopyroxene. These mafic-derived crystals show that the evolved mush incorporated crystals entrained from the mafic magma, such that the intermediate clots contain crystals from more than one magmatic environment.

Crystals in the intermediate clots are mutually touching and interlock along euhedral–subhedral boundaries (Fig. 11d–f), forming a crystal framework like that of the mafic clots. We therefore interpret the intermediate mineral clots as cumulate fragments of a second, more evolved crystal mush. We infer that this intermediate mush resided at shallower levels within the plumbing system (i.e., the shallower of the two seismic low-velocity zones), based on the expected general architecture of transcrustal magma systems rather than from thermobarometry constraints.

Reverse zoning in group two clinopyroxene crystals (Fig. 6c, d) records recharge of this intermediate reservoir by mafic magma. These reverse-zoned crystals occur only as macrocrysts, never within the mineral clots. The higher-Mg# bands overgrowing the more evolved group two clinopyroxene cores, commonly referred to as recharge bands (Palummo *et al.*, 2021), show that the crystals grew in a more mafic liquid than the one in which their cores formed (Palummo *et al.*, 2021; Mangler *et al.*, 2022). Critically, these high-Mg# bands also carry markedly higher $Cr_2O_3$ contents (0.12–0.24 wt%) than the adjacent low-Mg# bands (≤0.028 wt%; Supplementary Table S9, Supplementary Fig. S9). This co-variation of $Cr_2O_3$ with Mg# is characteristic of mafic recharge and separates it from other causes of reverse zoning such as degassing (Streck, 2008; Ubide & Kamber, 2018). Elevated $Cr_2O_3$ contents in high-Mg# recharge bands have similarly been documented in clinopyroxene crystals from Mt Etna (Streck, 2008; Ubide & Kamber, 2018). The revers-zoned clinopyroxene crystals therefore record mafic recharge of the intermediate reservoir in which the moderate-Mg# cores of group two clinopyroxene crystals had been growing. Additionally, the presence of multiple recharge bands in some crystals (Fig. 6d) points to multiple recharge events.

That reverse zoning is confined to macrocrysts and absent from the clot-hosted clinopyroxene suggests that crystals inside intact clots were shielded from direct contact with recharge magma, whereas free macrocrysts in the melt recorded these events. Group three plagioclase and orthopyroxene macrocrysts, which also grew *in situ* from the more evolved resident melt, do not show comparable recharge zoning. We interpret this to indicate that the reverse-zoned clinopyroxene macrocrysts and the *in situ* more evolved assemblage record different histories. The reverse-zoned clinopyroxene crystals encountered discrete pulses of mafic recharge, whereas the group three plagioclase and orthopyroxene crystals grew in a part of the more

evolved reservoir, or at a time, not directly affected by these recharge events.

Oscillatory zoning in group three plagioclase crystals records the internal dynamics of the intermediate mush. The oscillatory zoning consists of minor fluctuations in anorthite content that stay within the compositional range of group three plagioclase ($An_{45}$–$An_{55}$) (Fig. 5c). We attribute these subtle variations to convective movement within a melt-rich magma body that induced periodic changes in temperature, pressure, melt composition and water content (Ginibre *et al.*, 2002; Viccaro *et al.*, 2012; Ustunisik *et al.*, 2014).

A subset of our matrix glasses is more evolved than any of the compositions discussed so far. The most evolved glasses, with Mg#<30 and extending below Mg#20 and to rhyolitic $SiO_2$ contents (up to ~79 wt%), are not in equilibrium with any of the analysed crystals — neither the mafic cargo nor the *in situ* evolved assemblage. These glasses occur predominantly in the 1994 eruption products and, within that suite, define a distinct low-MgO, low-FeO, high-$SiO_2$ trend carried by the lava samples (S152972, S152973, S153126; Fig. S10), rather than by the volcanic bombs. We interpret these glasses not as a separate magma within the plumbing system but as residual interstitial melts produced by late-stage, post-eruptive groundmass crystallisation. As the lavas cooled slowly and degassed at or near the surface, extensive microlite crystallisation drove the remaining interstitial melt to progressively more evolved, silica-rich compositions, away from equilibrium with the phenocryst assemblage that grew in the reservoir (Bouvet de Maisonneuve *et al.,* 2015; Patia *et al.,* 2017). Their restriction to the slowly cooled lavas, their disequilibrium with all reservoir-derived crystals, and their extension to rhyolitic compositions along a fractionation-controlled trend are all consistent with this origin.

**Summary**

Together, our observations are consistent with the prevailing view of arc plumbing systems as heterogeneous, interconnected mush-dominated reservoirs (Cashman *et al.,* 2017; Edmonds *et al.,* 2019; Sparks *et al.,* 2019). The mafic mineral clots sample a basaltic mush, whereas the intermediate mineral clots sample a more evolved, andesitic-dacitic mush. Pulses of mafic magma were injected into the more evolved reservoir, where mafic crystals and cumulate fragments gain normal-zoned overgrowths after mixing, and where episodic recharge is recorded as reverse-zoned bands in group two clinopyroxene macrocrysts. The intermediate mineral clots themselves carry material inherited from the mafic mush – resorbed group two plagioclase cores that equilibrated with mafic melt, and orthopyroxene enclosing relict olivine. The intermediate mush is therefore composed of crystals grown locally as well as inherited cargo transported into the reservoir from elsewhere. Our thermobarometry cannot independently resolve whether these two mush domains are stored at distinct depths, but their compositional distinctness and the interchange between them are consistent with the vertically extensive, transcrustal mush systems inferred at many arc volcanoes. In line with this paradigm, and with the two low-velocity zones imaged beneath Rabaul (Bai & Greenhalgh, 2005; Itikarai, 2008), the mafic mush is plausibly stored at greater depth than the more intermediate mush.

## Evidence from magma mixing modelling

We modelled magma mixing in the post-Rabaul Pyroclastics eruption products with a simple, linear, two-endmember mixing model. We define the mafic endmember, interpreted as the recharge magma, as the average composition of the three most mafic samples known from Rabaul which are basaltic enclaves found in the 1878 (sample HPP003a) and 1937 (samples HPP075, HPP075a) eruption products (Patia, 2004; Cunningham *et al.*, 2009). We define the

felsic endmember as the average dacitic composition of the Rabaul Pyroclastics eruption products, which represents the last caldera-forming eruption (Fabbro *et al.*, 2020) (Table 3). We use the average Rabaul Pyroclastics dacite, rather than the single most silicic composition in the Rabaul dataset, because the endmember is intended to approximate the bulk composition of the resident more evolved reservoir into which mafic magma was injected, rather than the most fractionated melt pocket sampled. The most evolved individual analyses lie at the silicic extreme of the Rabaul Pyroclastics and are unlikely to represent the reservoir as a whole. An average dacite provides a more representative and more robust proxy that is also less sensitive to scatter in any single analysis. This choice is consistent with previous Rabaul mixing models, which likewise adopted a dacite similar to the bulk Rabaul Pyroclastics as the felsic endmember (Patia *et al.,* 2017; Fabbro *et al.,* 2020).

The calculated mixing line closely matches the whole-rock compositional trends displayed by the 1937, 1994, and 2014 Rabaul eruptions (Fig. 15). This correspondence suggests that eruption products could have been formed by mixing a mafic recharge magma with a composition similar to the basaltic Rabaul eruption products, into a magma reservoir of a more evolved magma with a composition similar to the Rabaul Pyroclastics dacites. For the 1994 eruption products that were analysed in this study, the mixing ratios of mafic to dacitic magma range from approximately 3:97 to 20:80, while the 2014 volcanic bombs display a ratio nearer 35:65. In contrast, the 1937 pumice analysed in this study is compositionally akin to the dacitic endmember and contains a negligible proportion of the mafic component (0:100). However, the apparent absence of a mafic component in the 1937 pumice analysed here likely reflects sampling bias: our suite comprises only dacitic pumice, whereas mafic enclaves and other mafic lithologies from the 1937 eruption have been documented (Patia, 2004).

Our modelling results are consistent with our interpretation that the minerals in the post-Rabaul Pyroclastics samples record evidence for mafic recharge into a resident dacitic reservoir. This indicates that all of the post-Rabaul Pyroclastics eruption products are effectively hybrid magmas containing evidence for the interactions of multiple melts and diverse crystal cargos.

Our findings are consistent with previous mixing modelling by Patia *et al.* (2017) and Fabbro *et al.* (2020). According to Patia *et al*. (2017), the 1994 whole-rock compositions could have been generated by mixing a basalt with 8–10 wt% MgO, similar to the 1937 basaltic enclaves, with a dacite that has ~1.8 wt% MgO and 64 wt% $SiO_2$. These compositions are similar to our endmember compositions. Fabbro *et al.* (2020) similarly reproduced the post-Rabaul Pyroclastics whole-rock trends with a basalt–dacite mixing line, and our result is fully consistent with theirs. Our approach differs, however, in how the endmembers are defined and in how the mixing model is corroborated. Fabbro *et al.* (2020) derived their mafic endmember by back-calculating from a fractional-crystallisation model (reversing the first crystallisation step of a WTZ basalt) and placed their felsic endmember at an assumed point on the modelled fractionation trend. We instead define both endmembers from measured Rabaul compositions (the average of the three most mafic samples known from Rabaul for the mafic endmember, and an average measured Rabaul Pyroclastics dacite for the felsic endmember) so that our mixing line is independent of any fractionation model. More importantly, we integrate the whole-rock mixing model with the mineral chemistry and textures of the crystal cargo (the two mineral-clot types and the group one to three mineral populations), which independently record the same basalt-into-dacite mixing at the crystal scale. That two methodologically independent approaches converge on the same basalt–dacite mixing relationship strengthens the interpretation.

In contrast, our results appear to contradict the model proposed by Bouvet de Maisonneuve *et al.* (2015), who attributed the 2006 eruption products to mixing between a dacitic magma similar to the Rabaul Pyroclastics and a different mafic endmember, a basalt akin to the eruption products of the adjacent mafic stratovolcano Kombiu with a lower MgO content of up to 6.5 wt%. In most major elements the Kombiu compositions fall off our post-Rabaul Pyroclastics mixing trend: at a given MgO they have distinctly lower $SiO_2$, $Na_2O$ and $K_2O$ and higher CaO and $Fe_2O_3$ than our mixing line, reflecting their more primitive, lower-alkali character (Fig. 15). The post-caldera eruption products analysed here, instead define a trend that projects toward the more evolved basaltic enclaves of the 1878 and 1937 eruptions rather than toward Kombiu. This supports our use of the enclave-based mafic endmember and is the basis for our inference that the mafic magma mixing into the post-caldera dacite is compositionally distinct from Kombiu basalt, in contrast to the model of Bouvet de Maisonneuve *et al.* (2015).

The mafic endmember of our mixing trend is defined by only three samples, and no eruption products span ~5–8 wt% MgO across the available Rabaul dataset, so this endmember is the least well constrained element of the model. Better sampling of primitive Rabaul compositions is needed to refine it.

Taken together, our mixing model advances the picture of the Rabaul plumbing system in three ways. First, by reproducing the whole-rock trends of the 1937, 1994 and 2014 eruptions from a single pair of endmembers, and by showing that the 2006 products belong to the same array, it establishes that basalt-into-dacite mixing is not an occasional feature but the persistent operating mode of the post-caldera system: every post-Rabaul Pyroclastics eruption sampled here is a hybrid of the same two magmas. Second, it constrains the resident felsic endmember

as a magma compositionally close to the Rabaul Pyroclastics dacite, implying that a persistent dacitic reservoir compositionally like the Rabaul Pyroclastics has been maintained at Rabaul throughout the post-caldera period and is repeatedly reactivated by mafic recharge. Third, because our endmembers are measured rather than modelled and are corroborated by the crystal cargo, the model identifies the mafic recharge magma as a Rabaul enclave-type basalt rather than a Kombiu-type basalt, refining which mantle-derived input drives the system. The recurrence of the same basalt–dacite mixing relationship across the post-caldera eruptions sampled here indicates that mixing between a persistent dacitic reservoir and recurrent mafic recharge is a fundamental and long-lived control on the compositions erupted at Rabaul.

## Oxygen fugacity conditions

Oxygen fugacity has a significant impact on magma differentiation and evolution, both in terms of the chemistry of the melt but also the rheology and, as a result, magma transport dynamics (Kelley & Cottrell, 2009; Kolzenburg *et al.*, 2018; Cottrell *et al.*, 2021). To our knowledge, there are no published measurements of oxygen fugacity conditions for Rabaul magmas. The only prior statement on redox conditions is from Bouvet de Maisonneuve *et al.* (2015), who described relatively poorly oxidising, tholeiitic differentiation conditions at around the NNO buffer, inferred from the tholeiitic trend (early Fe enrichment and delayed Fe–Ti oxide crystallisation) recorded by melt inclusions in the 2006 products. We note that this characterisation refers to the differentiation behaviour of the magma rather than to an absolute oxidation state below QFM: the NNO buffer itself lies above QFM (NNO ≈ QFM +1 at the relevant conditions; Frost, 1991), close to the typical range of arc magmas.

We used the oxybarometer of Arató and Audétat (2017) to calculate the oxygen fugacity for

the 1937, 1994 and 2014 eruptions at Rabaul. Our calculations yield oxygen fugacity conditions of ΔQFM ≈1 for all three eruptions. Given the uncertainty of the method — approximately ±0.3 log units at these conditions (≤ΔQFM+1.5; Arató & Audétat, 2017), and likely somewhat larger for ilmenite-undersaturated compositions, for which the model is less well validated — the apparent differences between the individual eruptions (spanning ΔQFM ≈ +0.9 to +1.3) are not resolved, and we treat them as indistinguishable. Rabaul magmas therefore record oxygen fugacities close to, and slightly above, the NNO buffer. These values are in agreement with the estimate of Bouvet de Maisonneuve *et al.* (2015). They also fall within the range of global arc magmas, which cluster around ΔQFM ≈ +1 (Cottrell *et al.,* 2021, and references therein). The origin of elevated oxygen fugacity in arc settings has been attributed to an oxidised mantle wedge caused by oxidising slab-derived fluids (Kelley & Cottrell, 2009; Kelley & Cottrell, 2012; Brounce *et al.*, 2014; Cottrell *et al.*, 2021). Rabaul magmas are therefore not reducing relative to their arc counterparts; the "poorly oxidising" character noted previously by Bouvet de Maisonneuve *et al.* (2015) reflects the tholeiitic differentiation path rather than an anomalously low absolute $fO_2$.

# Conclusions

We conducted a detailed and systematic investigation of the mineral chemistries and textures of products from the 1937, 1994 and 2014 eruptions at Rabaul. Our findings provide clear evidence that mafic recharge and magma mixing are fundamental processes within the Rabaul magma plumbing system. The magma compositions erupted at Rabaul are controlled by mafic recharge and recharge-driven mixing acting on a mush-dominated plumbing system, and the crystal cargo of the eruption products preserves a detailed record of these processes. By systematically characterising the mineral populations, mineral clots and zoning textures of the

1937, 1994 and 2014 eruptions, we have reconstructed how mafic magma is transferred into, and mixed with, the resident more evolved reservoir, and have used this record to refine the conceptual architecture of the Rabaul system.

The mineral populations resolve into a coherent record of two magmatic environments and their interaction. Group one plagioclase ($An_{85–95}$) and group one clinopyroxene, together with olivine, represent constituents of basaltic crystal mush. These crystals were remobilised and carried into a more evolved reservoir as mineral clots and macrocrysts, reflecting a range of mush fragment disaggregation. Their transfer and mixing with this more evolved, intermediate melt is recorded by low-An and low-Mg# overgrowth rims, quench-textured crystal clusters, and the peritectic replacement of olivine by orthopyroxene.

Intermediate mineral clots, composed of group two and group three plagioclase, group two clinopyroxene, orthopyroxene and Ti-magnetite, are fragments of this more evolved, andesitic–dacitic mush. Group three plagioclase, group two clinopyroxene and orthopyroxene crystallised *in situ* from the intermediate melt, in equilibrium with the intermediate-Mg# matrix glasses, and are compositionally identical to the rims on the mafic-derived crystals. Critically, the intermediate clots also contain mafic-derived crystals (resorbed group two plagioclase cores equilibrated with mafic melt, and orthopyroxene enclosing relict olivine) providing direct textural evidence that material from the mafic system was entrained into the intermediate mush, confirming interchange between the two reservoirs. The most evolved matrix glasses (Mg#<30) lie out of equilibrium with all reservoir-derived crystals and are interpreted as residual melts produced by late-stage groundmass crystallisation rather than as a reservoir component.

A two-endmember whole-rock mixing model, anchored on measured Rabaul compositions and applied consistently across eruptions, reproduces the compositional trends of the post-Rabaul Pyroclastics products and shows that basalt-into-dacite mixing is the persistent operating mode of the post-caldera system: each eruption sampled is a hybrid of the same resident dacite and a mafic recharge magma. The mafic endmember is best matched by a Rabaul enclave-type basalt rather than a Kombiu-type basalt, although the scarcity of primitive Rabaul samples leaves its composition relatively poorly constrained.

Clinopyroxene-only and clinopyroxene–liquid thermobarometry, applied here for the first time at Rabaul, yield pressures of 200 ± 50 MPa and temperatures of 1050 ± 50 °C, with a broad spread that may reflect either the limited precision of current thermobarometers for hydrous arc magmas or genuine crystallisation over an extended vertical interval. These methods cannot by themselves resolve the depths of the storage zones. Integrating our results with the two seismic low-velocity zones imaged beneath the caldera, we infer that the mafic mush is stored deeper than the resident more evolved reservoir, but this vertical arrangement is an inference from independent evidence rather than a result that can be resolved using our thermobarometry data. Our oxybarometry provides the first estimates of the redox state of Rabaul magmas, at $\Delta$QFM $\approx$ +1, placing them at typical arc values close to the NNO buffer rather than at anomalously reducing conditions.

Our observations are summarised in Figure 16, which shows schematically where and how the analysed crystal cargo formed and was transferred, in which Rabaul's magmas are stored in a heterogeneous but interconnected mush system, comprising at least a basaltic mush and a more evolved andesitic–dacitic mush, that is repeatedly reactivated by mafic recharge. Recharge disaggregates and remobilises mafic mush, transferring a mafic crystal cargo into the resident

more evolved reservoir, where mixing generates the hybrid andesitic–dacitic compositions that characterise every post-caldera eruption. The crystal cargo thus records not a single mixing event but the recurrent interaction of mafic and more evolved magmas that governs the compositions Rabaul erupts. Given the persistence of this process across the historical eruptions and the continuing hazard posed by this densely populated caldera, the crystal-scale record offers a means of tracking the recharge and mixing that drive its activity, and provides a framework against which future eruptive products, and the geophysical structure of the system, can be interpreted.

## Acknowledgements

This work was supported by a University of Manchester doctoral scholarship to Melina Höhn. We thank Ben Ellis and Jasper Berndt-Gerdes for assistance with XRF and electron microprobe analyses. We thank Martin Mangler and an anonymous reviewer for their constructive suggestions, and Valentin Troll for editorial handling. MEH acknowledges support from NERC grant NE/X/013642/1. BMK acknowledges fieldwork funding via the Alfred P. Sloan Foundation's support of the Deep Carbon Observatory Deep Earth Carbon Degassing program (DECADE), and the Centre for Observation and Modelling of Earthquakes, Volcanoes and Tectonics (COMET).

## Data availability

Data underlying this article are available in the article and its online supplementary material as well as in the EarthChem Library data repository, at https://doi.org/10.60520/IEDA/114601.

# References


Anderson, A. T. (1976). Magma mixing: petrological process and volcanological tool. *Journal of Volcanology and Geothermal Research* **1**, 3-33.

Annen, C., Blundy, J. D. & Sparks, R. S. J. (2006). The genesis of intermediate and silicic magmas in deep crustal hot zones. *Journal of Petrology* **47**, 505-539.

Arató, R. & Audétat, A. (2017). FeTiMM – A new oxybarometer for mafic to felsic magmas. *Geochemical Perspectives Letters*, 19-23.

Bai, C.-y. & Greenhalgh, S. (2005). 3D multi-step travel time tomography: Imaging the local, deep velocity structure of Rabaul volcano, Papua New Guinea. *Physics of the Earth and Planetary Interiors* **151**, 259-275.

Baldwin, S. L., Fitzgerald, P. G. & Webb, L. E. (2012). Tectonics of the New Guinea Region. *Annual Review of Earth and Planetary Sciences* **40**, 495-520.

Bernard, O. & Bouvet de Maisonneuve, C. (2020). Controls on eruption style at Rabaul, Papua New Guinea – Insights from microlites, porosity and permeability measurements. *Journal of Volcanology and Geothermal Research* **406**.

Bouvet de Maisonneuve, C., Costa, F., Patia, H. & Huber, C. (2015). Mafic magma replenishment, unrest and eruption in a caldera setting: insights from the 2006 eruption of Rabaul (Papua New Guinea). *Geological Society, London, Special Publications* **422**, 17-39.

Brounce, M. N., Kelley, K. A. & Cottrell, E. (2014). Variations in $Fe^{3+}/\sum Fe$ of mariana arc basalts and mantle wedge $fO_2$. *Journal of Petrology* **55**, 2513-2536.

Campbell, I. H. (1978). Some problems with the cumulus theory. *Lithos* **11**, 311-323.

Cashman, K. V. & Sparks, R. S. J. (2013). How volcanoes work: A 25 year perspective. *Geological Society of America Bulletin* **125**, 664-690.

Cashman, K. V., Sparks, R. S. & Blundy, J. D. (2017). Vertically extensive and unstable magmatic systems: A unified view of igneous processes. *Science* **355**.

Coombs, M. L. & Gardner, J. E. (2004). Reaction rim growth on olivine in silicic melts: Implications for magma mixing. *American Mineralogist* **89**, 748-758.

Coote, A. C. & Shane, P. (2016). Crystal origins and magmatic system beneath Ngauruhoe volcano (New Zealand) revealed by plagioclase textures and compositions. *Lithos* **260**, 107-119.

Costa, F., Dohmen, R. & Chakraborty, S. (2008). Time scales of magmatic processes from modeling the zoning patterns of crystals. *Reviews in Mineralogy and Geochemistry* **69**, 545-594.

Cottrell, E., Birner, S. K., Brounce, M., Davis, F. A., Waters, L. E. & Kelley, K. A. (2021). Oxygen fugacity across tectonic settings. In: Moretti, R. & Neuville, D. R. (eds.) *Magma Redox*

*Geochemistry*, 33-61.

Cunningham, H. S., Turner, S. P., Dosseto, A., Patia, H., Eggins, S. M. & Arculus, R. J. (2009). Temporal variations in U-series disequilibria in an active caldera, Rabaul, Papua New Guinea. *Journal of Petrology* **50**, 507-529.

Davidson, J. P., Morgan, D. J., Charlier, B. L. A., Harlou, R. & Hora, J. M. (2007). Microsampling and isotopic analysis of igneous rocks: Implications for the study of magmatic systems. A*nnual Review of Earth and Planetary Sciences* **35**, 273-311.

Delph, J. R., Ward, K. M., Zandt, G., Ducea, M. N. & Beck, S. L. (2017). Imaging a magma plumbing system from MASH zone to magma reservoir. *Earth and Planetary Science Letters* **457**, 313-324.

Edmonds, M., Cashman, K. V., Holness, M. & Jackson, M. (2019). Architecture and dynamics of magma reservoirs. *Philosophical Transactions of the Royal Society A: Mathematical, Physical and Engineering Sciences* **377**, 20180298.

Fabbro, G. N., McKee, C. O., Sindang, M. E., Eggins, S. M. & Bouvet de Maisonneuve, C. (2020). Variable mafic recharge across a caldera cycle at Rabaul, Papua New Guinea. *Journal of Volcanology and Geothermal Research* **393**.

Fearnley, C. J., Bird, D. K., Haynes, K., McGuire, W. J. & Jolly, G. (2018). *Observing the Volcano World*: Springer.

Finlayson, D. M., Gudmundsson, O., Itikarai, I., Nishimura, Y. & Shimamura, H. (2003). Rabaul volcano, Papua New Guinea: seismic tomographic imaging of an active caldera. *Journal of Volcanology and Geothermal Research* **124**, 153-171.

Frey, H. & Lange, R. (2011). Phenocryst complexity in andesites and dacites from the Tequila volcanic field, Mexico: resolving the effects of degassing vs. magma mixing. *Contributions to Mineralogy and Petrology* **162**, 415-445.

Frost, B. R. (1991). Introduction to oxygen fugacity and its petrologic importance. *Reviews in Mineralogy and Geochemistry* **25**, 1–9.

Ginibre, C., Kronz, A. & Wörner, G. (2002). High-resolution quantitative imaging of plagioclase composition using accumulated backscattered electron images: new constraints on oscillatory zoning. *Contributions to Mineralogy and Petrology* **142**, 436-448.

Global Volcanism Program. (1994a). Report on Rabaul (Papua New Guinea) (Venzke, E., ed.). *Bulletin of the Global Volcanism Network, 19:9*: Smithsonian Institution.

Global Volcanism Program. (1994b). Report on Rabaul (Papua New Guinea) (Wunderman, R., ed.). *Bulletin of the Global Volcanism Network, 19:10*: Smithsonian Institution.

Global Volcanism Program. (2006). Report on Rabaul (Papua New Guinea) (Wunderman, R., ed.). *Bulletin of the Global Volcanism Network, 31:9*: Smithsonian Institution.

Global Volcanism Program. (2007). Report on Rabaul (Papua New Guinea) (Wunderman, R., ed.). *Bulletin of the Global Volcanism Network, 32:6*: Smithsonian Institution.

Global Volcanism Program. (2011). Report on Rabaul (Papua New Guinea) (Wunderman, R., ed.). *Bulletin of the Global Volcanism Network, 36:7*: Smithsonian Institution.

Global Volcanism Program. (2013). Report on Rabaul (Papua New Guinea) (Wunderman, R., ed.). *Bulletin of the Global Volcanism Network, 38.10*: Smithsonian Institution.

Global Volcanism Program. (2014). Report on Rabaul (Papua New Guinea) (GVP Staff, ed.). *Bulletin of the Global Volcanism Network, 39.8*: Smithsonian Institution.

Global Volcanism Program. (2017). Report on Rabaul (Papua New Guinea) (Crafford, A.E., and Venzke, E., eds.). *Bulletin of the Global Volcanism Network, 42:2*: Smithsonian Institution.

Global Volcanism Program. (2021). Report on Rabaul (Papua New Guinea) (Sennert, S., ed.). *Weekly Volcanic Activity Report, 13 October–19 October 2021*: Smithsonian Institution and US Geological Survey.

Global Volcanism Program. (2024). Report on Rabaul (Papua New Guinea) (Senner, S., ed.). *Weekly Volcanic Activity Report, 30 October–5 November 2024*: Smithsonian Institution and US Geological Survey.

Hammer, J. E., Sharp, T. G. & Wessel, P. (2010). Heterogeneous nucleation and epitaxial crystal growth of magmatic minerals. *Geology* **38**, 367-370.

Heming, R. F. (1974). Geology and petrology of Rabaul Caldera, Papua New Guinea. *Geological Society of America Bulletin* **85**, 1253–1264.

Heming, R. F. (1977). Mineralogy and proposed P-T paths of basaltic lavas from Rabaul caldera, Papua New Guinea. *Contributions to Mineralogy and Petrology* **61**, 15–33.

Hepworth, L. N., O'Driscoll, B., Gertisser, R., Daly, J. S. & Emeleus, C. H. (2018). Linking in situ crystallization and magma replenishment via sill intrusion in the Rum Western Layered Intrusion, NW Scotland. *Journal of Petrology* **59**, 1605-1642.

Hohl, S. V., Schuth, S., Münker, C., König, S., Garbe-Schönberg, D. & Kuduon, J. (2022). Geochemical evolution of the Rabaul volcanic complex, Papua New Guinea – Insights from HFSE, Sr-Nd-Hf, and Fe isotopes. *Lithos* **408-409**.

Holm, R. J., Rosenbaum, G. & Richards, S. W. (2016). Post 8 Ma reconstruction of Papua New Guinea and Solomon Islands: Microplate tectonics in a convergent plate boundary setting. *Earth-Science Reviews* **156**, 66–81.

Holness, M. B., Vukmanovic, Z. & O'Driscoll, B. (2023). The formation of chromite chains and clusters in igneous rocks. *Journal of Petrology* **64**.

Horn, E. L., Taylor, R. N., Gernon, T. M., Stock, M. J. & Farley, E. M. R. (2022). Composition and petrology of a mush-bearing magma reservoir beneath Tenerife. *Journal of Petrology* **63**.

Humphreys, M. C. S., Blundy, J. D. & Sparks, R. S. J. (2006). Magma evolution and open-system processes at Shiveluch Volcano: Insights from phenocryst zoning. *Journal of Petrology* **47**, 2303-2334.

Humphreys, M. C. S., Christopher, T. & Hards, V. (2009). Microlite transfer by disaggregation

of mafic inclusions following magma mixing at Soufrière Hills volcano, Montserrat. *Contributions to Mineralogy and Petrology* **157**, 609-624.

Itikarai, I. (2008). The 3-D structure and earthquake locations at Rabaul Caldera, Papua New Guinea. *A Thesis submitted for the degree of Master of Philosophy, The Australian National University.*

Jaupert, C. & Tait, S. (1995). Dynamics of differentiation in magma reservoirs. *Journal of Geophysical Research: Solid Earth* **100**, 17615-17636.

Johnson, R. W. (2013). *Fire Mountains of the Islands: A History of Volcanic Eruptions and Disaster Management in Papua New Guinea and the Solomon Islands*: ANU Press.

Jorgenson, C., Higgins, O., Petrelli, M., Begue, F. & Caricchi, L. (2022). A Machine learning-based approach to clinopyroxene thermobarometry: model optimization and distribution for use in Earth Sciences. *Journal of Geological Research: Solid Earth* **127**, e2021JB022904.

Kelley, K. A. & Cottrell, E. (2009). Water and the oxidation state of subduction zone magmas. *Science* **325**, 605-607.

Kelley, K. A. & Cottrell, E. (2012). The influence of magmatic differentiation on the oxidation state of Fe in a basaltic arc magma. *Earth and Planetary Science Letters* **329-330**, 109-121.

Kolzenburg, S., Di Genova, D., Giordano, D., Hess, K. U. & Dingwell, D. B. (2018). The effect of oxygen fugacity on the rheological evolution of crystallizing basaltic melts. *Earth and Planetary Science Letters* **487**, 21-32.

Kruger, W. & Latypov, R. (2020). Fossilized solidification fronts in the Bushveld Complex argue for liquid-dominated magmatic systems. *Nature Communications* **11**.

Lanari, P., Markmann, T., Laughton, J. & Tedeschi, M. (2023). XMapTools 4.2. Zenodo.

Lissenberg, C. J., MacLeod, C. J. & Bennett, E. N. (2019). Consequences of a crystal mush-dominated magma plumbing system: a mid-ocean ridge perspective. *Philosophical Transactions of the Royal Society A: Mathematical, Physical and Engineering Sciences* **377**.

Mangler, M. F., Petrone, C. M. & Prytulak, J. (2022). Magma recharge patterns control eruption styles and magnitudes at Popocatépetl volcano (Mexico). *Geology* **50**, 366-370.

McKee, C. O., Baillie, M. G. & Reimer, P. J. (2015). A revised age of ad 667–699 for the latest major eruption at Rabaul. *Bulletin of Volcanology* **77**.

McKee, C. O. & Duncan, R. A. (2016). Early volcanic history of the Rabaul area. *Bulletin of Volcanology* **78**.

McKee, C. O., Lowenstein, P. L., Saint Ours, P., Talai, B., Itikarai, I. & Mori, J. J. (1984). Seismic and ground deformation crises at Rabaul Caldera: Prelude to an eruption? *Bulletin Volcanologique* **47**, 397-411.

Morgavi, D., Laumonier, M., Petrelli, M. & Dingwell, D. B. (2022). Decrypting magma mixing in igneous systems. *Reviews in Mineralogy and Geochemistry* **87**, 607-638.

Mori, J. & McKee, C. (1987). Outward-dipping ring-fault structure at rabaul caldera as shown by earthquake locations. *Science* **235**, 193-195.

Nairn, I. A., McKee, C. O., Talai, B. & Wood, C. P. (1995). Geology and eruptive history of the Rabaul Caldera area, Papua New Guinea. *Journal of Volcanology and Geothermal Research* **69**, 255–284.

Nairn, I. A., Wood, C. P., Talai, B. & Mckee, C. O. (1989). Rabaul Caldera, Papua New Guinea —125,000 reconnaissance geological map and eruption history. New Zealand Geological Survey.

Namur, O., Montalbano, S., Bolle, O. & Vander Auwera, J. (2020). Petrology of the April 2015 eruption of Calbuco Volcano, southern Chile. *Journal of Petrology* **61**.

Neave, D. A., Bali, E., Guðfinnsson, G. H., Halldórsson, S. A., Kahl, M., Schmidt, A.-S. & Holtz, F. (2019). Clinopyroxene–liquid equilibria and geothermobarometry in natural and experimental tholeiites: the 2014–2015 Holuhraun Eruption, Iceland. *Journal of Petrology* **60**, 1653-1680.

Neave, D. A., Stewart, A., Hartley, M. E. & Namur, O. (2024). Iron valence systematics in clinopyroxene crystals from ocean island basalts. *Contributions to Mineralogy and Petrology* **179**.

Palummo, F., Mollo, S., Petrone, C. M., Ellis, B. S., De Astis, G., Nazzari, M., Scarlato, P. & Bachmann, O. (2021). Decoding multiple zoning patterns in clinopyroxene phenocrysts at Vulcano Island: A record of dynamic crystallization through interconnected reservoirs. *Lithos* **406-407**.

Patia, H. (2004). Petrology and geochemistry of the recent eruption history at Rabaul Caldera. *University of Papua New Guinea, Port Moresby*.

Patia, H., Eggins, S. M., Arculus, R. J., McKee, C. O., Johnson, R. W. & Bradney, A. (2017). The 1994–2001 eruptive period at Rabaul, Papua New Guinea: Petrological and geochemical evidence for basalt injections into a shallow dacite magma reservoir, and significant $SO_2$ flux. *Journal of Volcanology and Geothermal Research* **345**, 200–217.

Paulatto, M., Moorkamp, M., Hautmann, S., Hooft, E., Morgan, J. V. & Sparks, R. S. J. (2019). Vertically extensive magma reservoir revealed from joint inversion and quantitative interpretation of seismic and gravity data. *Journal of Geophysical Research: Solid Earth* **124**, 11170-11191.

Petrelli, M., Caricchi, L. & Perugini, D. (2020). Machine learning thermo−barometry: Application to clinopyroxene−bearing magmas. *Journal of Geophysical Research: Solid Earth* **125**.

Plail, M., Barclay, J., Humphreys, M. C. S., Edmonds, M., Herd, R. A. & Christopher, T. E. (2014). Chapter 18 Characterization of mafic enclaves in the erupted products of Soufrière Hills Volcano, Montserrat, 2009 to 2010. *Geological Society, London, Memoirs* **39**, 343-360.

Putirka, K. D. (2008). Thermometers and barometers for volcanic systems. *Reviews in Mineralogy and Geochemistry* **69**, 61-120.

Rasmussen, D. J., Plank, T. A., Roman, D. C. & Zimmer, M. M. (2022). Magmatic water content controls the pre-eruptive depth of arc magmas. *Science* **375**, 1169-1172.

Reubi, O. & Blundy, J. (2009). A dearth of intermediate melts at subduction zone volcanoes and the petrogenesis of arc andesites. *Nature* **461**, 1269-1273.

Roggensack, Williams, Schaefer & Parnell. (1996). Volatiles from the 1994 eruptions of Rabaul: understanding large caldera systems. *Science* **273**, 490–493.

Ruprecht, P., Bergantz, G. W., Cooper, K. M. & Hildreth, W. (2012). The crustal magma storage system of Volcán Quizapu, Chile, and the effects of magma mixing on magma diversity. *Journal of Petrology* **53**, 801-840.

Ruprecht, P., Simon, A. C. & Fiege, A. (2020). The survival of mafic magmatic enclaves and the timing of magma recharge. *Geophysical Research Letters* **47**.

Saunders, S., Tenor, E., Wakawa, J. & Nohou, J. (2023). Twenty-two years of GPS monitoring at Rabaul Caldera, a narrative history. *Geosciences* **13**.

Saunders, S. J. (2001). The shallow plumbing system of Rabaul caldera: a partially intruded ring fault? *Bulletin of Volcanology* **63**, 406-420.

Schwindinger, K. R. & Anderson, A. T. (1989). Synneusis of Kilauea Iki olivines. *Contributions to Mineralogy and Petrology* **103**, 187-198.

Sparks, S. R. J., Sigurdsson, H. & Wilson, L. (1977). Magma mixing: a mechanism for triggering acid explosive eruptions. *Nature* **267**, 315-318.

Sparks, R. S. J., Annen, C., Blundy, J. D., Cashman, K. V., Rust, A. C. & Jackson, M. D. (2019). Formation and dynamics of magma reservoirs. *Philosophical Transactions of the Royal Society A: Mathematical, Physical and Engineering Sciences* **377**, 20180019.

Streck, M. J. (2008). Mineral textures and zoning as evidence for open system processes. *Reviews in Mineralogy and Geochemistry* **69**, 595-622.

Takach, M. K., Tepley, F. J., Harpel, C. J., Aguilar, R. & Rivera, M. (2024). To mix or not to mix: details of magma storage, recharge, and remobilization during the Pacheco stage at Misti Volcano, Peru (≤21–2 ka). *Journal of Petrology* **65**.

Tsuchiyama, A. (1986). Experimental study of olivine-melt reaction and its petrological implications. *Journal of Volcanology and Geothermal Research* **29**, 245-264.

Ubide, T., Galé, C., Larrea, P., Arranz, E., Lago, M. & Tierz, P. (2014). The relevance of crystal transfer to magma mixing: a case study in composite dykes from the Central Pyrenees. *Journal of Petrology* **55**, 1535-1559.

Ubide, T. & Kamber, B. S. (2018). Volcanic crystals as time capsules of eruption history. *Nature communications* **9**, 326.

Ubide, T., Neave, D. A., Petrelli, M. & Longpré, M.-A. (2021). Editorial: crystal archives of magmatic processes. *Frontiers in Earth Science* **9**.

Ustunisik, G., Kilinc, A. & Nielsen, R. L. (2014). New insights into the processes controlling compositional zoning in plagioclase. *Lithos* **200-201**, 80-93.

Vance, J. A. (1969). On synneusis. *Contributions to Mineralogy and Petrology* **24**, 7-29.

Viccaro, M., Giuffrida, M., Nicotra, E. & Ozerov, A. Y. (2012). Magma storage, ascent and recharge history prior to the 1991 eruption at Avachinsky Volcano, Kamchatka, Russia: Inferences on the plumbing system geometry. *Lithos* **140-141**, 11-24.

Waters, L. & Lange, R. (2017). An experimental study of $^{Fe2+-Mg}K_D$ between orthopyroxene and rhyolite: a strong dependence on $H_2O$ in the melt. *Contributions to Mineralogy and Petrology* **172**.

Wieser, P. E., Vukmanovic, Z., Kilian, R., Ringe, E., Holness, M. R., Maclennan, J. & Edmonds, M. (2019). To sink, swim, twin, or nucleate: A critical appraisal of crystal aggregation processes. *Geology* **47**, 948-952.

Wieser, P., Petrelli, M., Lubbers, J., Wieser, E., Ozaydin, S., Kent, A. & Till, C. (2022). Thermobar: An open-source Python3 tool for thermobarometry and hygrometry. *Volcanica* **5**, 349-384.

Wieser, P., Kent, A. & Till, C. (2023a). Barometer behaving badly II: A critical evaluation of Cpx-only and Cpx-liq thermobarometry in variably-hydrous arc magmas.

Wieser, P. E., Kent, A. J. R., Till, C. B., Donovan, J., Neave, D. A., Blatter, D. L. & Krawczynski, M. J. (2023b). Barometers behaving badly I: assessing the influence of analytical and experimental uncertainty on clinopyroxene thermobarometry calculations at crustal conditions. *Journal of Petrology* **64**.

Wood, C. P., Nairn, I. A., Mckee, C. O. & Talai, B. (1995). Petrology of the Rabaul Caldera area, Papua New Guinea. *Journal of Volcanology and Geothermal Research* **69**, 285–302.

Zellmer, G. F., Sakamoto, N., Matsuda, N., Iizuka, Y., Moebis, A. & Yurimoto, H. (2016). On progress and rate of the peritectic reaction Fo + $SiO_2$ → En in natural andesitic arc magmas. *Geochimica et Cosmochimica Acta* **185**, 383-393.

**Table 1:** Recent eruption history of Rabaul (modified after Nairn *et al.*, 1995; Patia *et al.*, 2017; Fabbro *et al.*, 2020).

| date/age (CE) | source of eruption | description | volume ($km^3$) | VEI |
|---|---|---|---|---|
| 2014 | Tavurvur | Strombolian activity with lava flows in the beginning, then change to vulcanian eruption style | ? | 3 |
| 2006 | Tavurvur | Sub-Plinian eruption with ash fall, debris flow from partial collapse of northwest flank, change to strombolian style with lava effusion | 0.2 | 4 |
| 1994 | Vulcan and Tavurvur | Plinian eruption at Vulcan with intra-caldera pyroclastic flows and ash fall; strombolian eruption at Tavurvur with lava flow | V: 0.26<br>T: 0.04 | 4 |
| 1937–1943 | Vulcan and Tavurvur | Sub-Plinian eruption at Vulcan including interaction with seawater; discrete vulcanian event at Tavurvur | 0.005 | 4 |
| 1878 | Vulcan and Tavurvur | Submarine, pyroclastic cone-building eruption at Vulcan; strombolian and vulcanian activity at Tavurvur | V: 0.3<br>T: 0.05 | 3 |
| 1791 | Tavurvur | Lava and pyroclastic eruptions | ? | 2 |
| 1767 | Rabalanakaia or Tavurvur | Lava and pyroclastic eruptions | ? | 2 |

**Table 2:** Samples analysed in this study. Modal mineralogy is calculated on a vesicle-free basis.

| Eruption | Vent | Sample Location | Sample | Rock Type | Vesicles (vol%) | Cryst. | Mineral Assemblage (Vol%) | | | | | |
|---|---|---|---|---|---|---|---|---|---|---|---|---|
| | | | | | | | gl | plg | cpx | opx | ol | mgt |
| 1937 | Vulcan | 4.27253 S, 152.16901 E | RBL_1937_pum | pumice | 80–85 | 0.15 | 85 | 13 | 1.0 | 0.5 | | 0.5 |
| 1994 | Tavurvur | flanks | S152971 | volcanic bomb | 58 | 0.30 | 70 | 20 | 7.0 | 1.5 | 0.5 | 1.0 |
| | Tavurvur | flanks | S152972 | lava | 19 | 0.36 | 64 | 25 | 4.0 | 3.0 | 2.0 | 2.0 |
| | Tavurvur | flanks | S152973 | lava | 7 | 0.25 | 75 | 18 | 4.0 | 1.0 | 1.0 | 1.0 |
| | Tavurvur | flanks | S153126 | lava | 4 | 0.39 | 61 | 27 | 7.0 | 2.0 | 2.0 | 1.0 |
| | Vulcan | flanks | S153127 | lava | 17 | 0.29 | 71 | 23 | 3.0 | 2.0 | <0.1 | 1.0 |
| 2014 | Tavurvur | 4.23025 S, 152.20342 E | VB_IA* | volcanic bomb | | | | | | | | |
| 2014 | Tavurvur | 4.23025 S, 152.20342 E | VB_IB | volcanic bomb | 61 | 0.38 | 62 | 28 | 6.5 | 2.0 | 1.0 | 0.5 |

Cryst. = crystallinity, gl = matrix glass, plg = plagioclase, cpx = clinopyroxene, opx = orthopyroxene, ol = olivine, mgt = Ti-magnetite
*no mineralogy data available for sample VB_IA

**Table 3:** Mafic and felsic compositions used for magma mixing modelling. The mafic endmember is the average composition of the most mafic samples known from Rabaul (Patia, 2004; Cunningham *et al.*, 2009). The felsic endmember is a dacite from the Rabaul Pyroclastics eruption (Fabbro *et al.*, 2020).

| | $SiO_2$ | $TiO_2$ | $Al_2O_3$ | $Fe_2O_3$ | MnO | MgO | CaO | $Na_2O$ | $K_2O$ | $P_2O_5$ | Total |
|---|---|---|---|---|---|---|---|---|---|---|---|
| **mafic comp.** | 50.57 | 0.80 | 15.73 | 10.01 | 0.17 | 8.10 | 11.95 | 2.34 | 0.75 | 0.15 | 100.58 |
| **felsic comp.** | 62.47 | 0.91 | 15.64 | 6.57 | 0.16 | 2.04 | 4.88 | 4.52 | 2.49 | 0.31 | 99.98 |

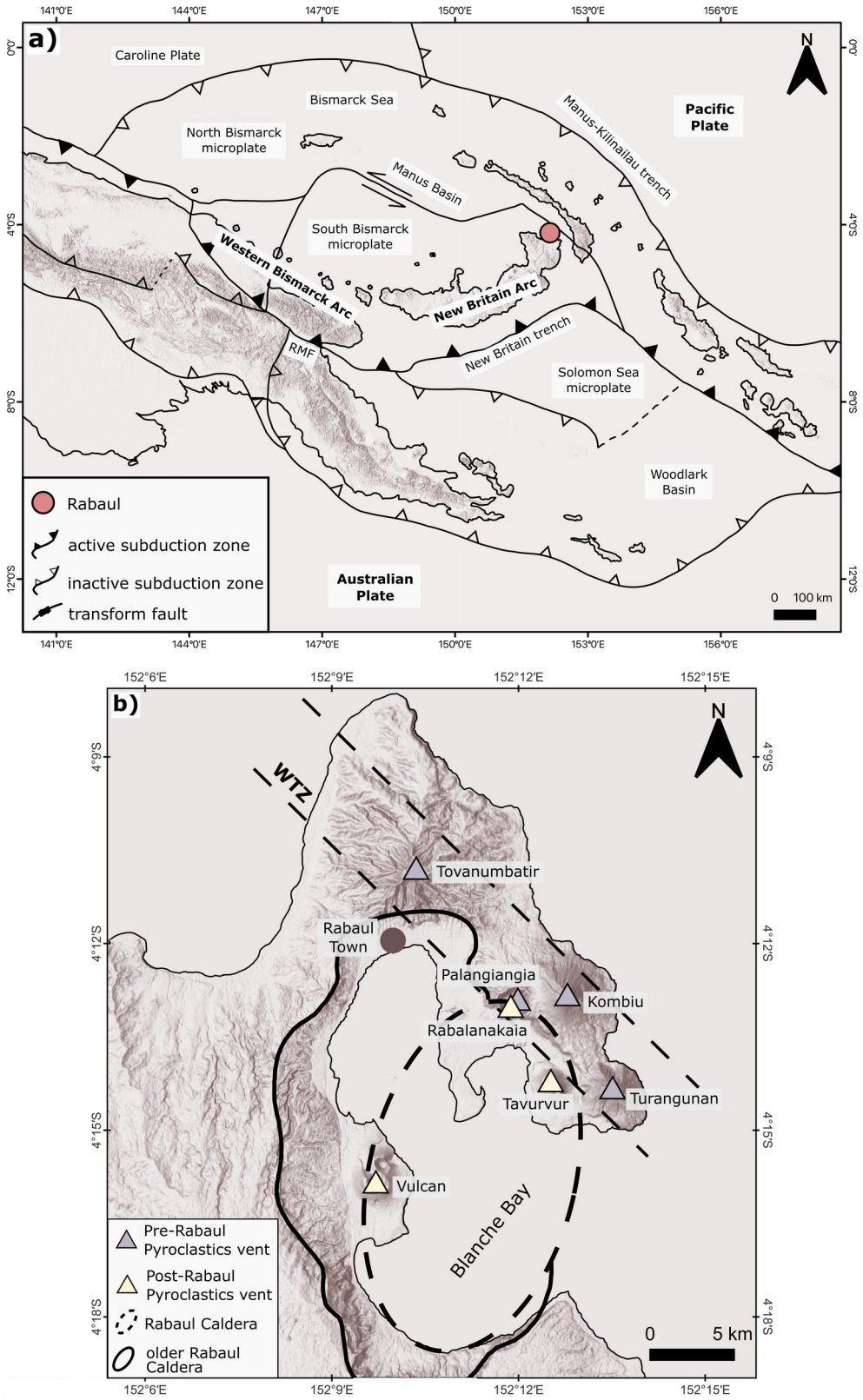


**Figure 1: a)** Tectonic setting of New Britain Island (tectonic elements after Holm *et al.,* 2019; topographic map: Esri World Topo Map). RMF = Ramu-Marham fault. **b)** Overview of the Rabaul Caldera Complex (vent and caldera locations after Fabbro *et al.,* 2020; topographic map: Esri World Topo Map). WTZ = Watom-Turangunan-Zone.

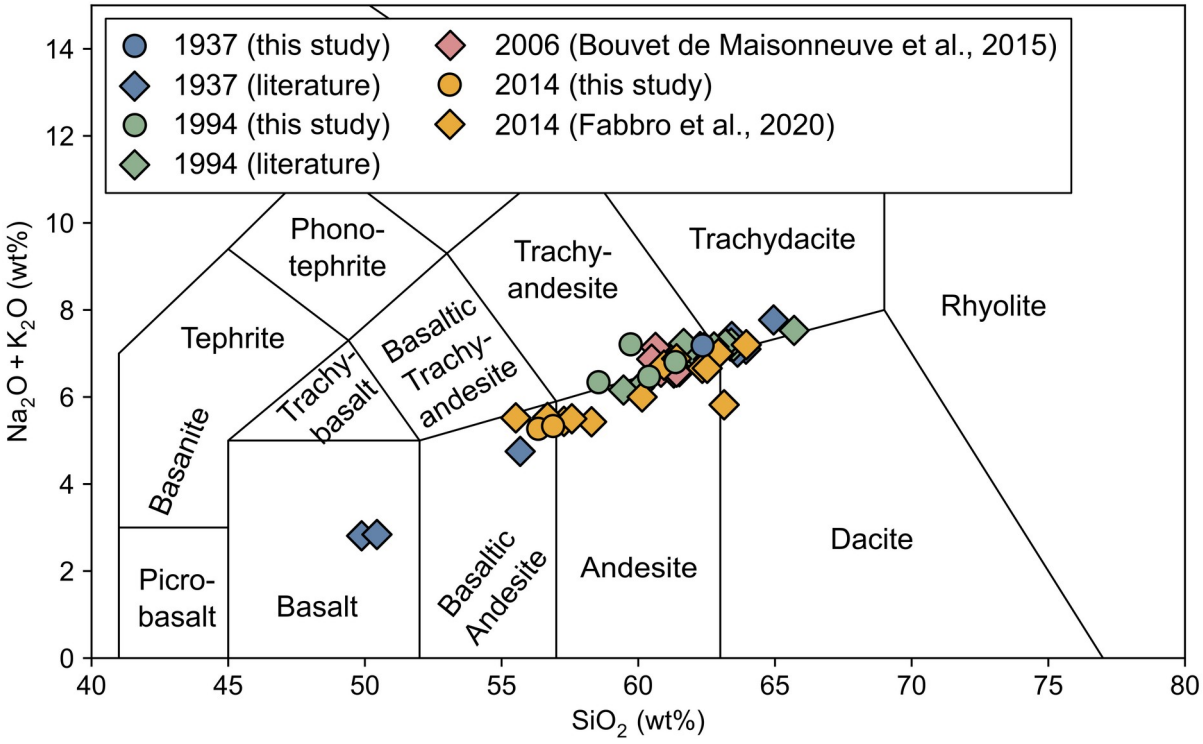


**Figure 2:** TAS diagrams comparing whole-rock compositions of samples analysed in this study for eruptions from the years 1937, 1994 and 2014 with literature data for the post-Rabaul Pyroclastics eruptions (literature data from Heming, 1974; Nairn *et al.*, 1989; Patia, 2004; Cunningham *et al.*, 2009; Bouvet de Maisonneuve *et al.*, 2015; Patia *et al.*, 2017; Bernard & Bouvet de Maisonneuve, 2020, Fabbro *et al.*, 2020; Hohl *et al.*, 2022).

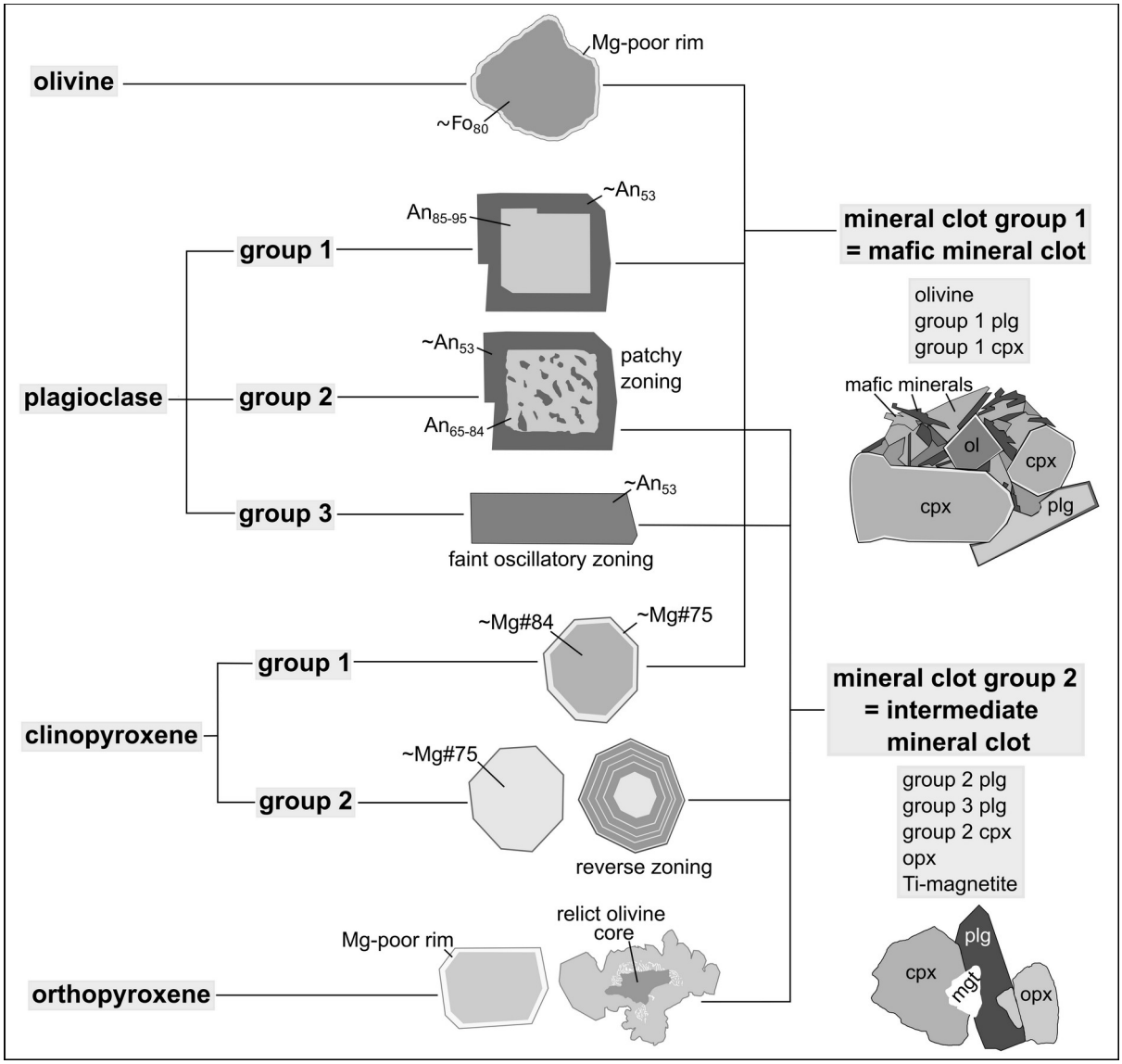


**Figure 3:** Sketch showing the different textural/chemical groups of macrocrysts in the Rabaul eruption products and how they can be found together in the two different groups of mineral clots. plg = plagioclase, cpx = clinopyroxene, opx = orthopyroxene.

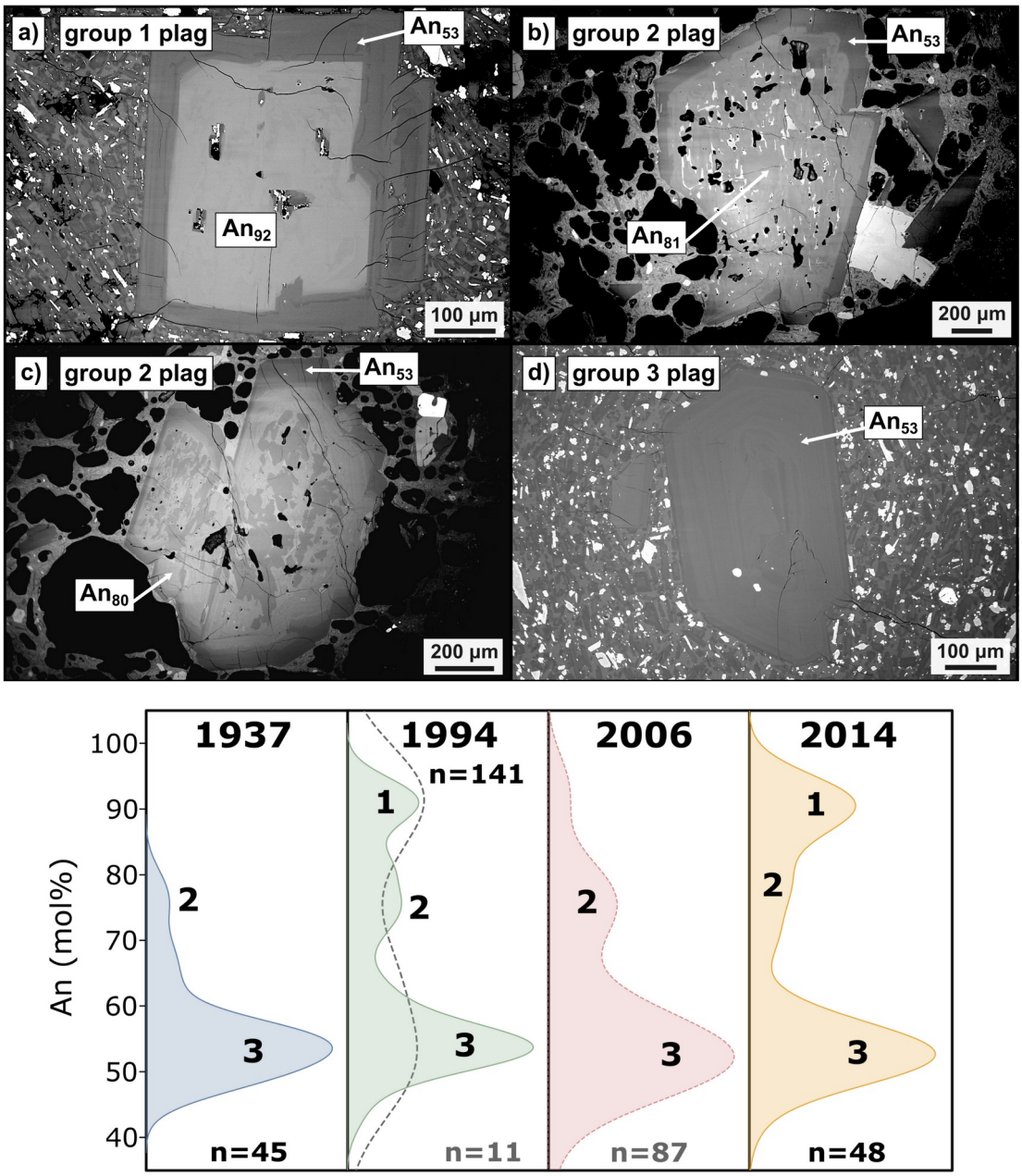


**Figure 4:** **Upper:** Backscattered electron images showing **a)** group one plagioclase with An-rich core and An-poorer rim, **b)** group two plagioclase with An-rich core and patchy zones of lower An composition, **c)** group two plagioclase with An-rich, resorbed core and An-poorer rim, **d)** group three plagioclase with faint oscillatory zoning. All images are of products from the 1994 eruption. **Lower:** Kernel density plots showing the distribution of plagioclase core compositions for the different eruptions of Rabaul. The numbers mark the peaks of group one, group two, and group three plagioclase core compositions. Coloured shaded curves are data from this study; grey dotted curves are literature data. (Patia, 2004; Cunningham *et al.*, 2009; Bouvet de Maisonneuve *et al.*, 2015). Number of analyses are given in black (this study) and grey (literature data).

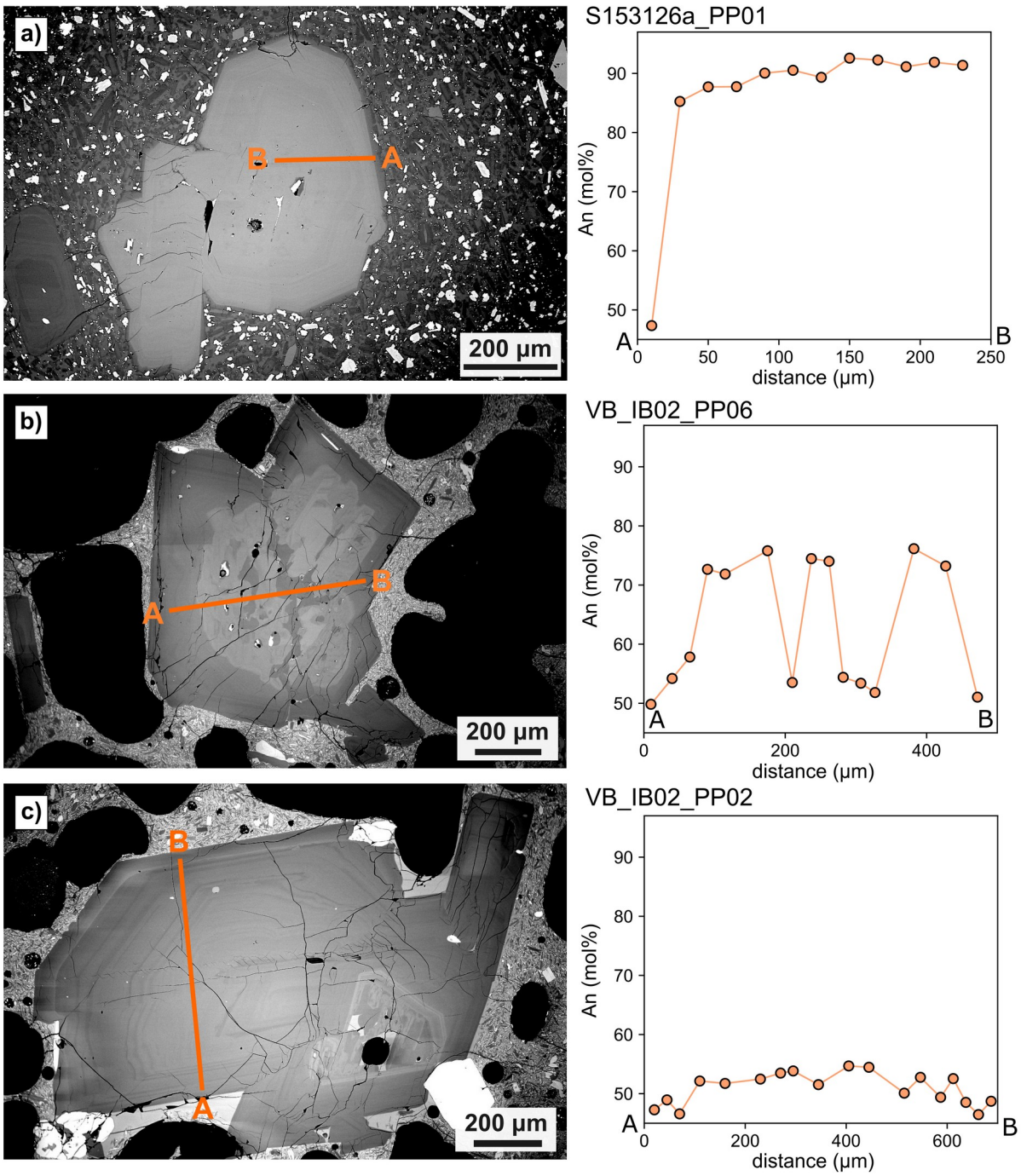


**Figure 5:** Examples of compositional zoning profiles in **a)** group one plagioclase from the 1994 Rabaul eruption, **b)** group two plagioclase from the 2014 Rabaul eruption, **c)** group three plagioclase from the 2014 Rabaul eruption. Orange lines across crystals mark the locations of profiles.

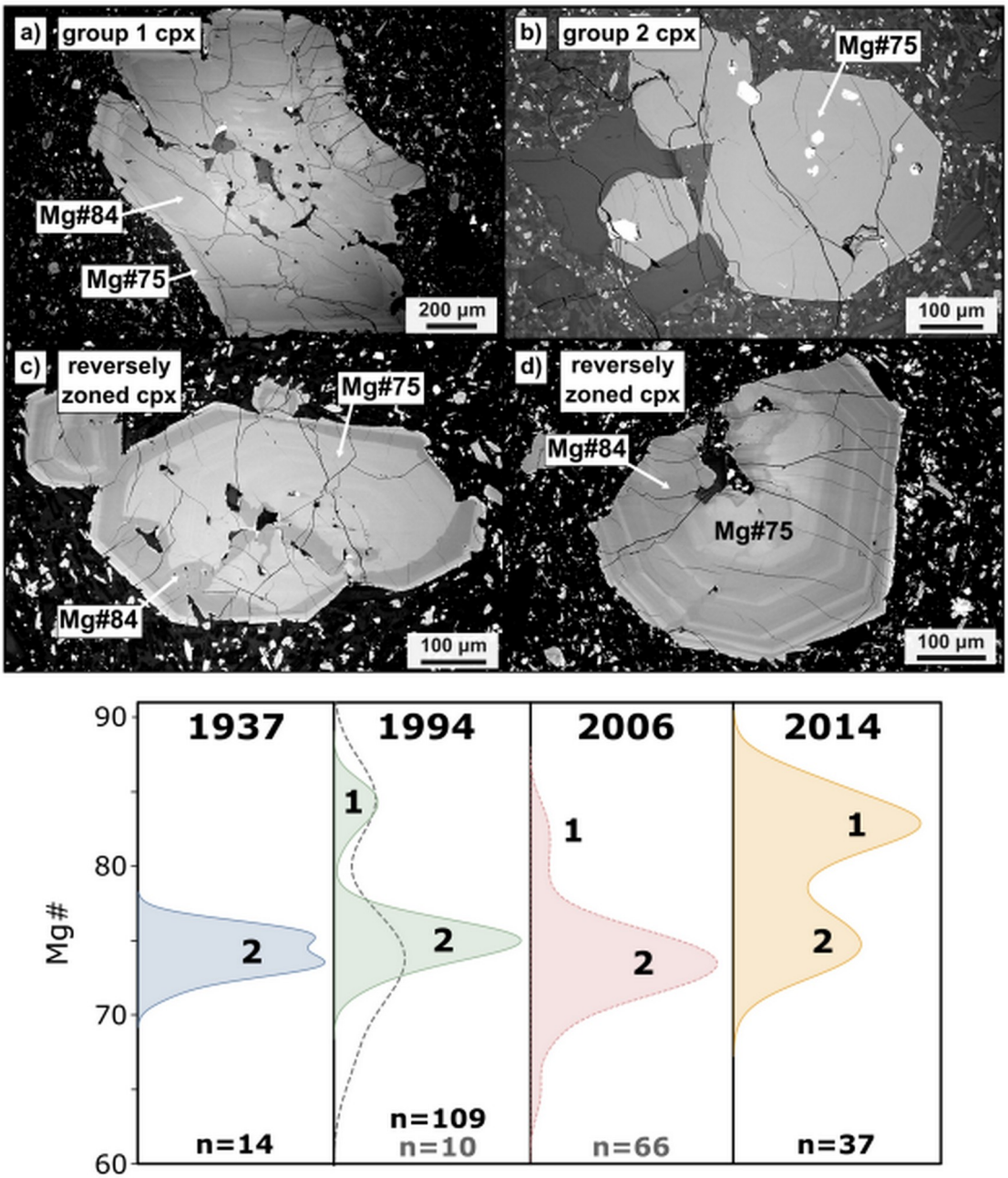


**Figure 6:** **Upper**: Backscattered electron images showing **a)** group one clinopyroxene with a low-Mg# rim, **b)** group two clinopyroxene, **c–d)** group two clinopyroxene with reverse zoning in the 1994 eruption products. **Lower**: Kernel density plots showing the distribution of clinopyroxene core compositions from the different eruptions of Rabaul. The numbers mark the peaks of group one and group two clinopyroxene cores. Coloured shaded curves are data from this study; grey dotted curves are literature data (Heming, 1977; Patia, 2004; Cunningham *et al.*, 2009; Bouvet de Maisonneuve *et al.*, 2015). Number of analyses are given in black (this study) and grey (literature data).

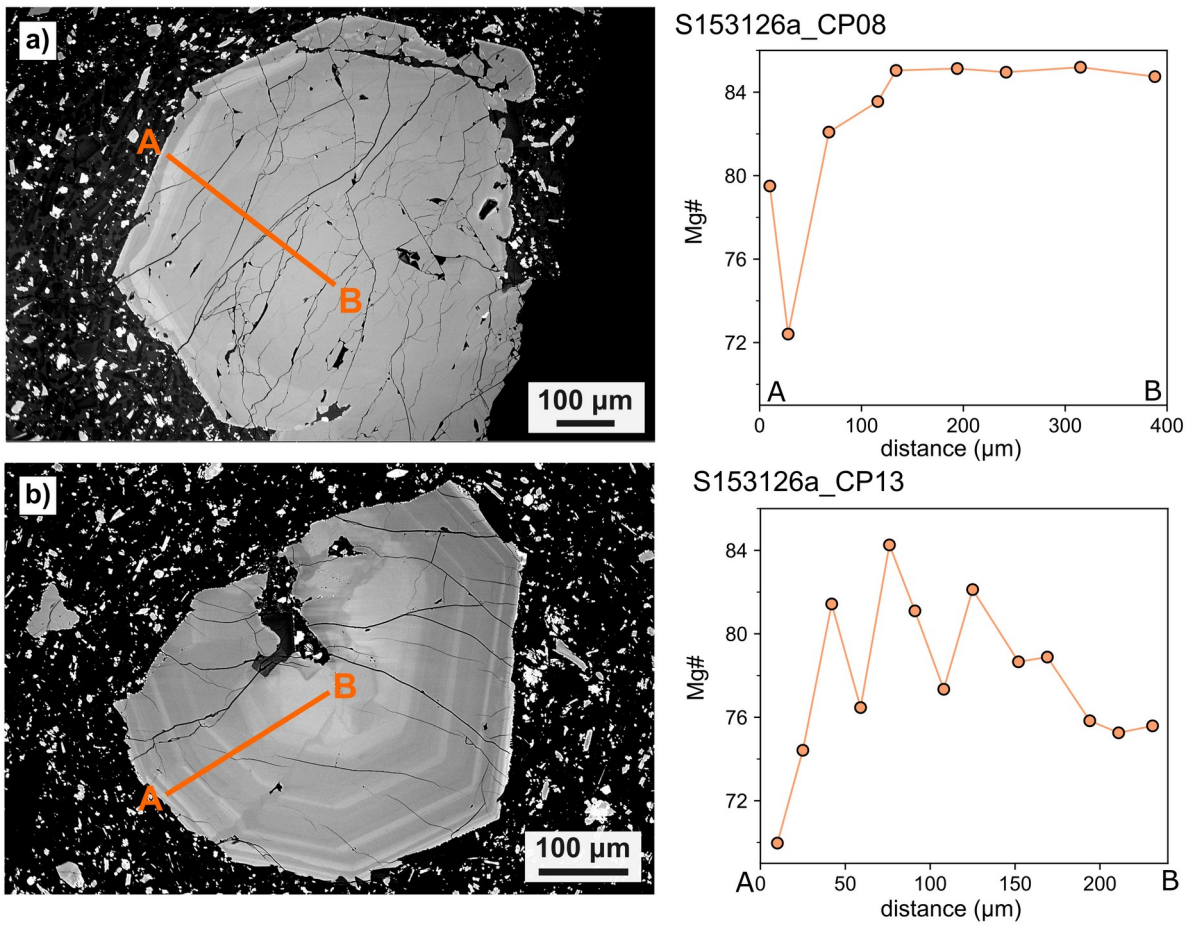


**Figure 7:** Examples of compositional zoning profiles across clinopyroxene from the 1994 Rabaul eruptions. **a)** Group one clinopyroxene with a rim that is lower in Mg# content, **b)** reversely zoned clinopyroxene with a group two core and overgrown by alternating bands of group one and group two clinopyroxene. Orange lines across crystals mark the locations of profiles.

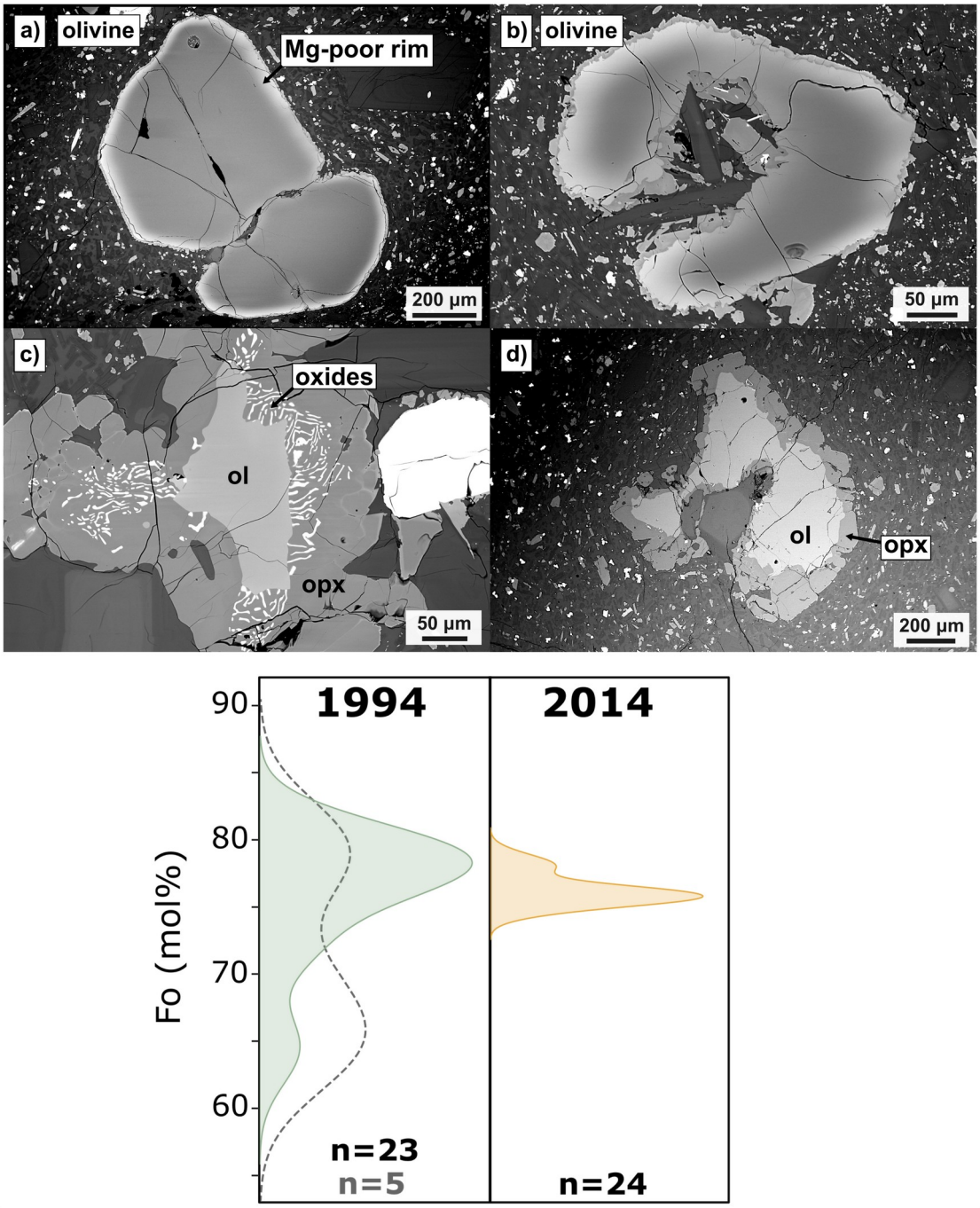


**Figure 8:** **Upper**: Backscattered electron images showing **a–b)** olivine with thin, Mg-poor rim; **c–d)** olivine (ol) replaced by orthopyroxene (opx). All images are of 1994 Rabaul eruption products. **Lower**: Kernel density plots showing the distribution of olivine core compositions from the different eruptions of Rabaul. Coloured shaded curves are data from this study; grey dotted curves are literature data (Heming, 1977; Patia, 2004; Cunningham *et al.*, 2009). Number of analyses are given in black (this study) and grey (literature data).

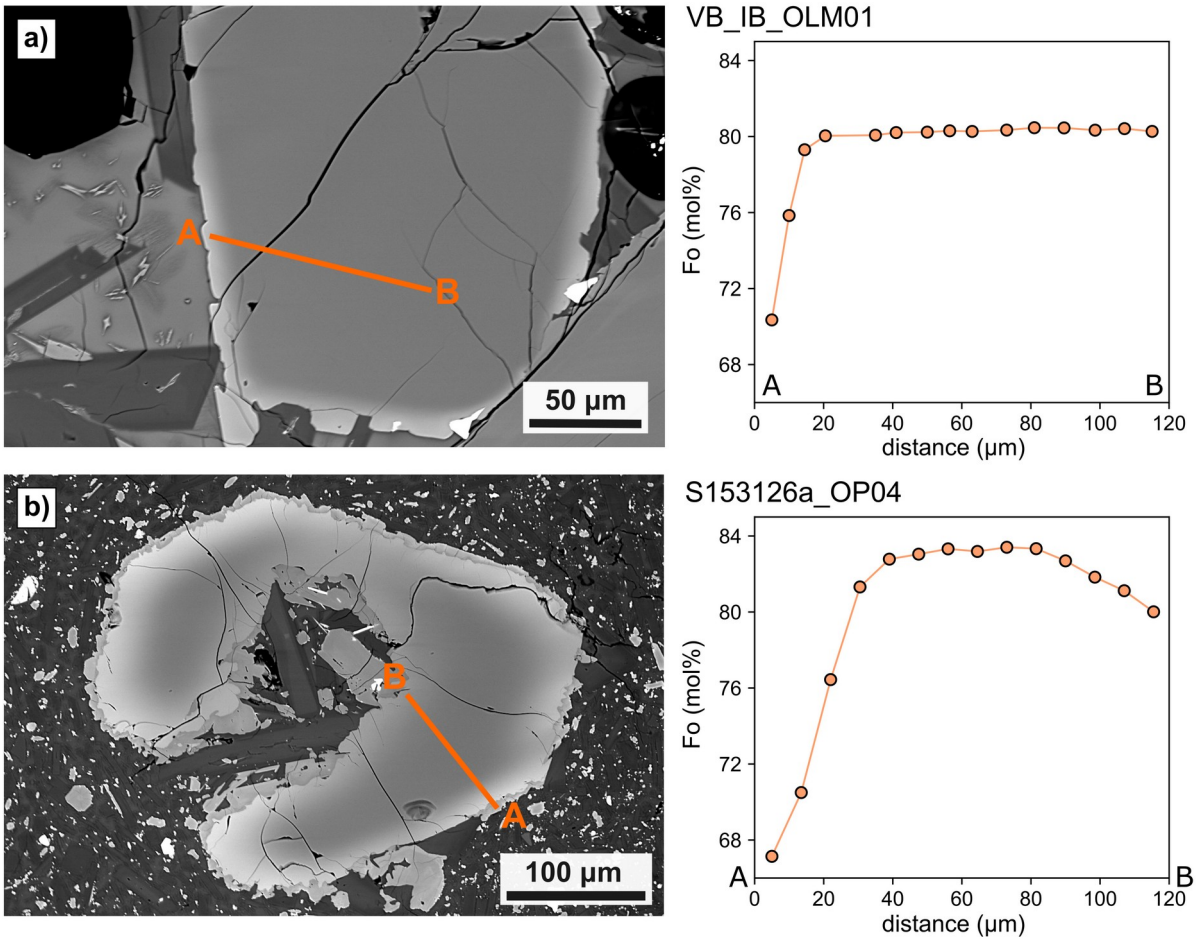


**Figure 9:** Examples of compositional zoning profiles across olivine crystals from the Rabaul eruptions in olivine with thin, bright, Mg-poor rim from **a)** the 2014 and **b)** eruption products. Orange lines across crystals mark the locations of profiles.

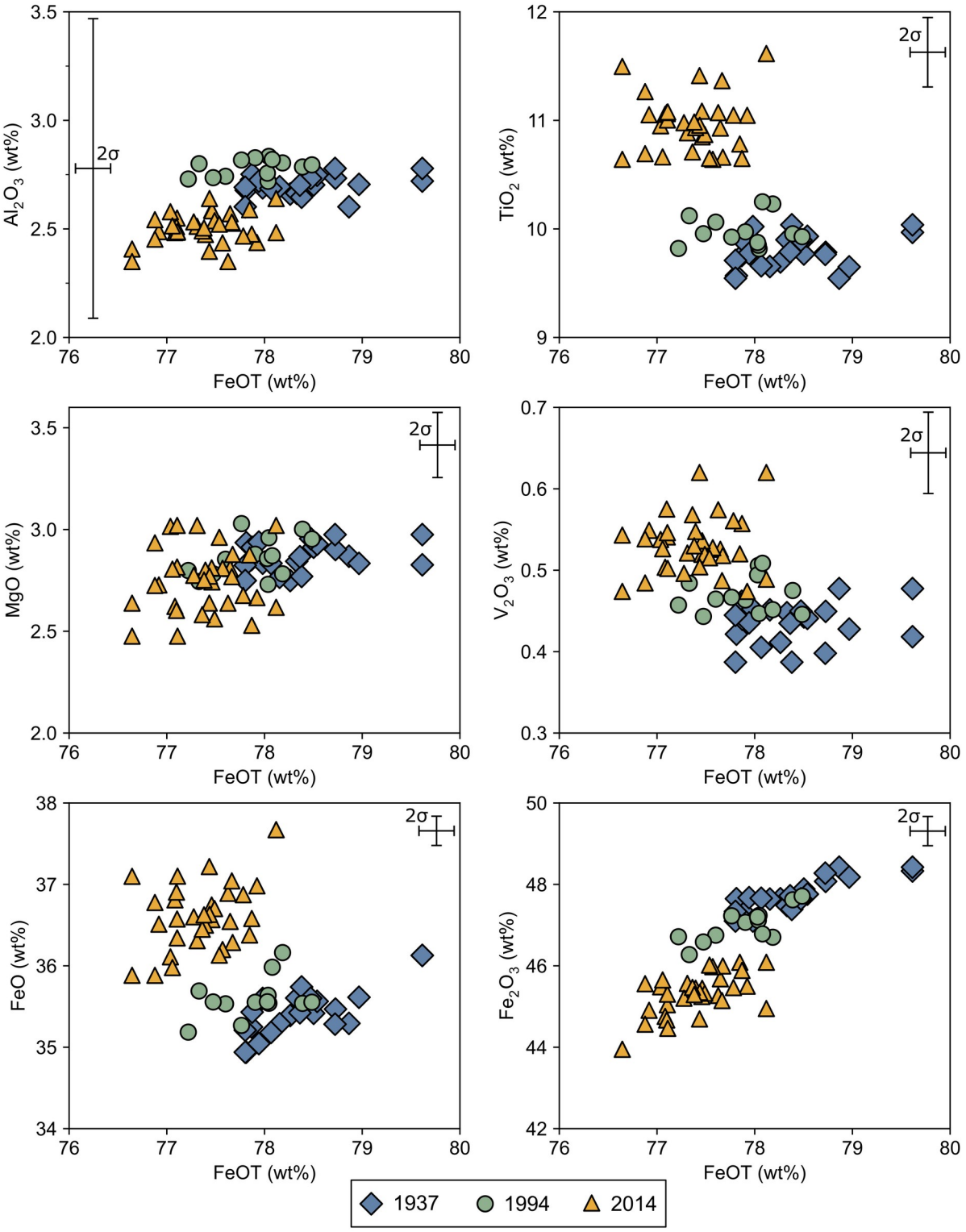


**Figure 10:** Ti-magnetite compositions in the 1937, 1994 and 2014 eruption products of Rabaul. Error bars indicate 2σ uncertainties.

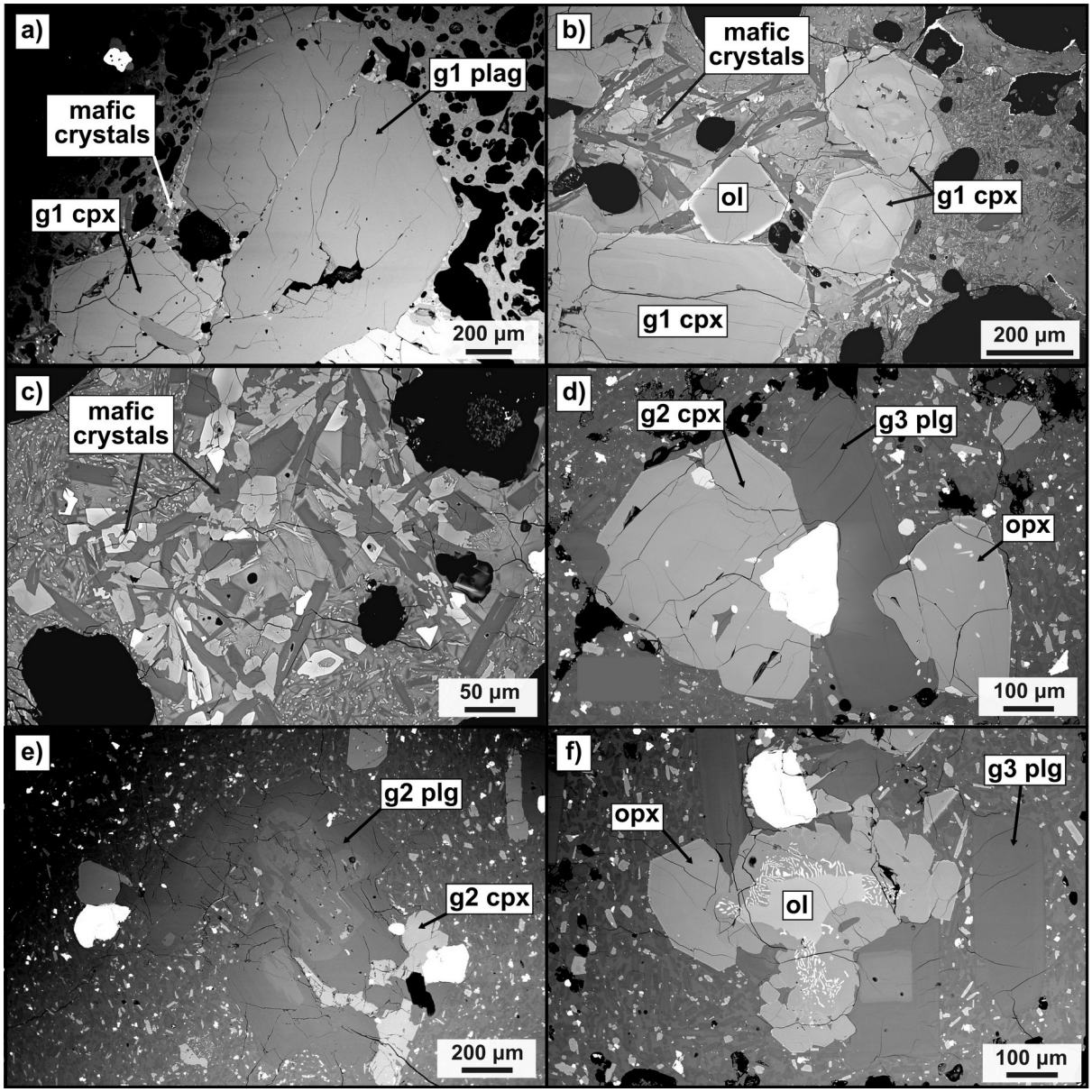


**Figure 11:** Backscattered electron images showing **a)** edge of mafic mineral clot with group one plagioclase and group one clinopyroxene as well as olivine-plagioclase-clinopyroxene clusters with mafic compositions, **b)** edge of mafic mineral clot with group one clinopyroxene and olivine rimmed by olivine-clinopyroxene-plagioclase clusters, **c)** clusters of small olivine, plagioclase and clinopyroxene crystals with mafic compositions, all in products of the 2014 eruption. **d)** Intermediate mineral clot with group two clinopyroxene, Ti-magnetite, group three plagioclase and orthopyroxene (from left to right), **e)** intermediate mineral clot with group two plagioclase and group to clinopyroxene, **f)** intermediate mineral clot with group three plagioclase and orthopyroxene with a relict olivine core, all in 1994 Rabaul eruption products.

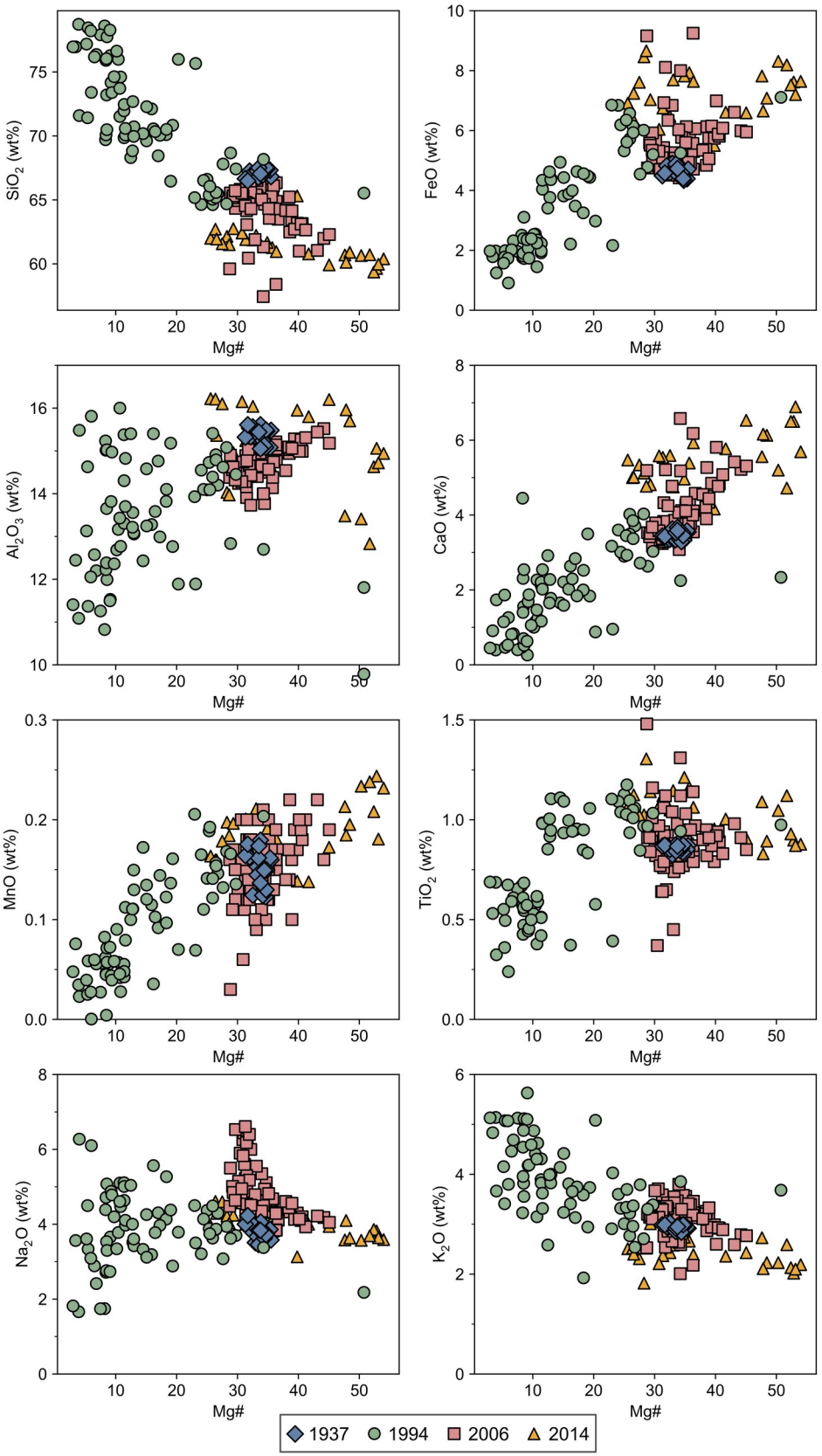


**Figure 12:** Matrix glass compositions from the 1937, 1994, 2006 and 2014 eruption products of Rabaul (data for 2006 eruption from Bouvet de Maisonneuve *et al.*, 2015).

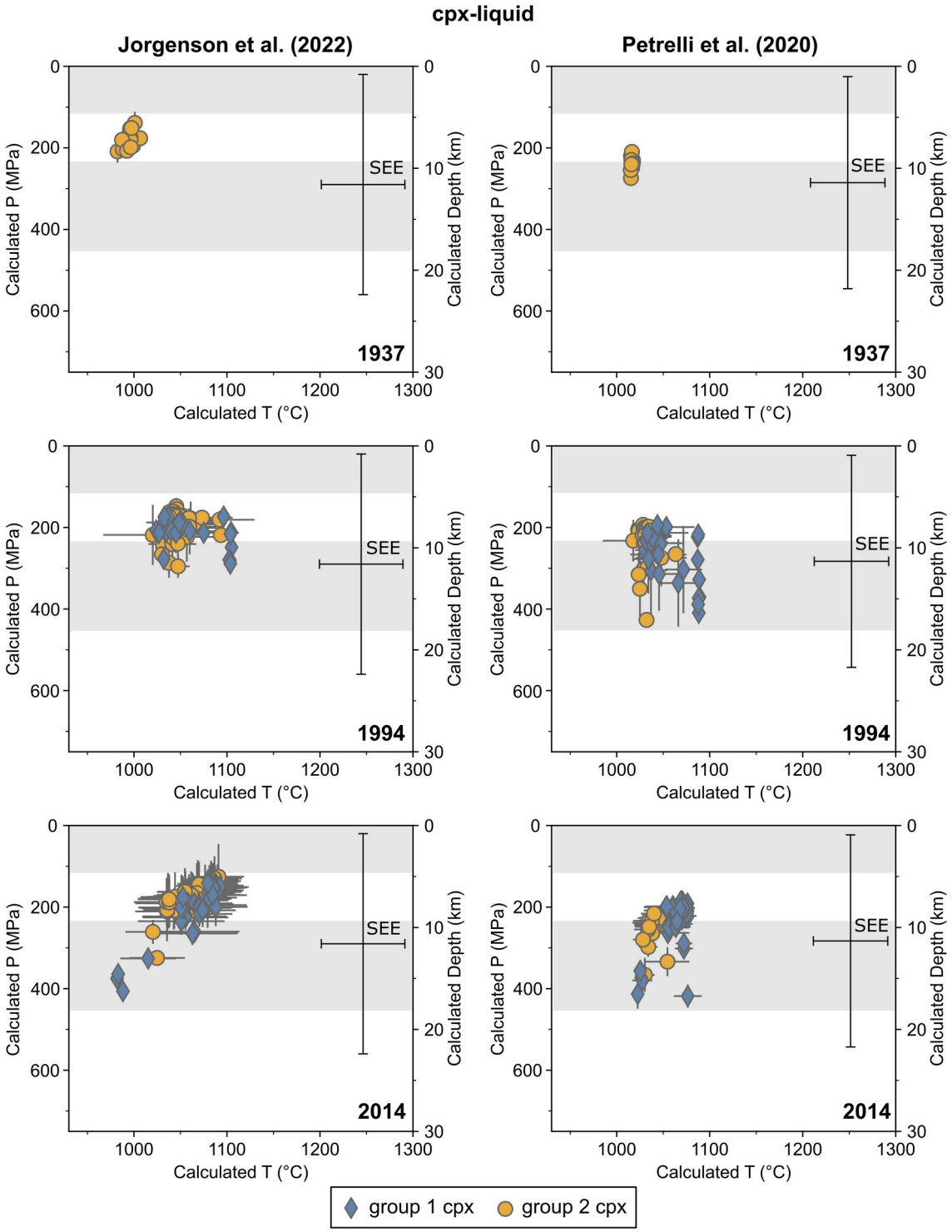


**Figure 13:** Clinopyroxene-liquid pressure-temperature results (group one clinopyroxene in blue diamonds, group two clinopyroxene in yellow circles) for the 1937, 1994 and 2014 eruptions of Rabaul calculated with the thermobarometry models of Jorgenson *et al.* (2022) (left) and Petrelli *et al.* (2020) (right) implemented in Thermobar (Wieser *et al.*, 2022). A $H_2O$ content of 2.5 wt% was assumed for calculations with the models of Petrelli *et al.* (2020). Diamonds/circles and error bars represent mean and standard deviation of all P-T estimates for one individual clinopyroxene crystal. Standard error estimates (SEE) for the thermobarometry models are shown with the crosses. The grey bars indicate low velocity zones in a depth of 0–4 km and 9–18 km (Bai & Greenhalgh, 2005).

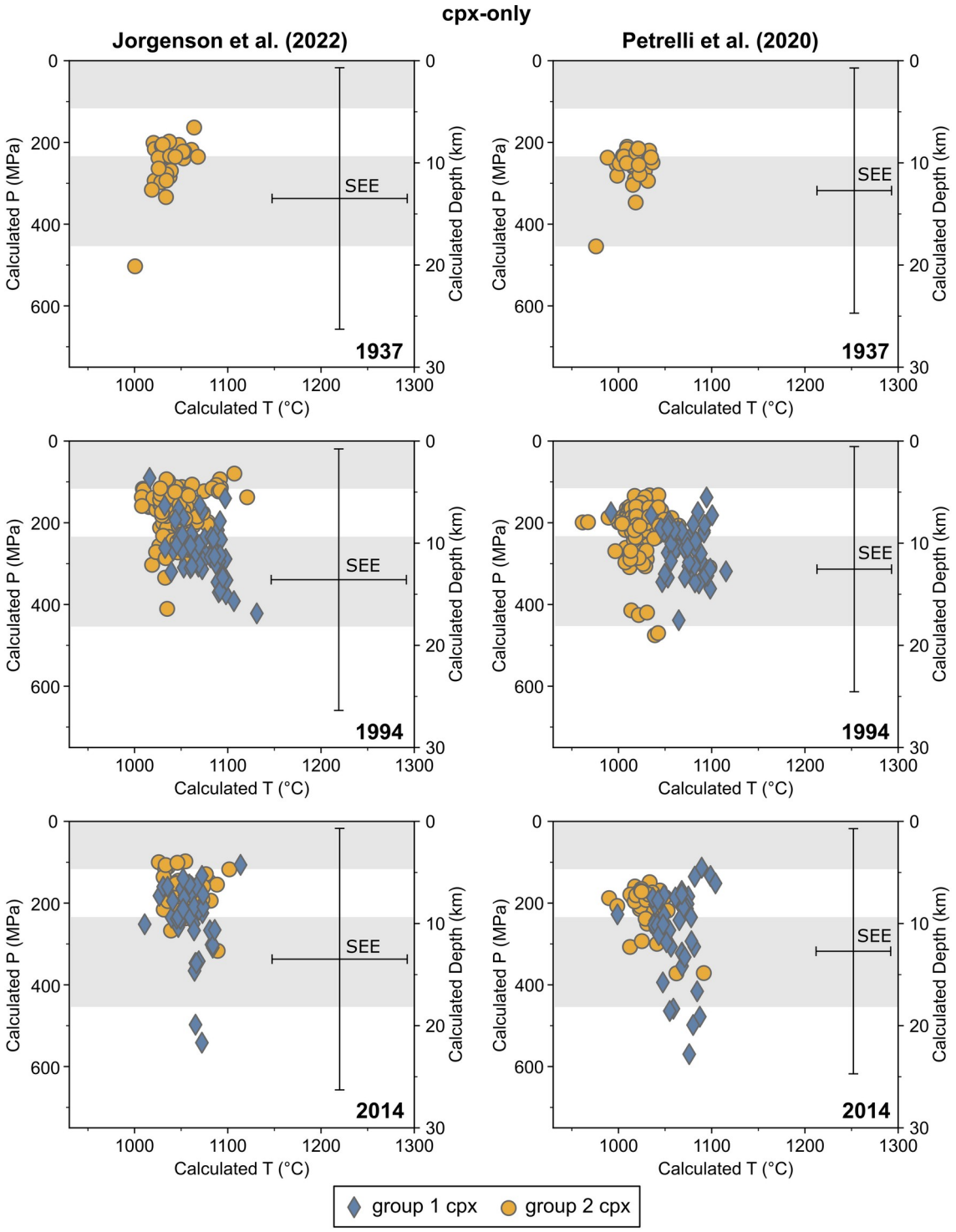


**Figure 14:** Clinopyroxene-only pressure-temperature results (group one clinopyroxene in blue diamonds, group two clinopyroxene in yellow circles) for the 1937, 1994 and 2014 eruptions of Rabaul calculated with the thermobarometry models of Jorgenson *et al.* (2022) (left) and Petrelli *et al.* (2020) (right) implemented in Thermobar (Wieser *et al.*, 2022). A $H_2O$ content of 2.5 wt% was assumed for calculations with the models of Petrelli *et al.* (2020). Standard error estimates (SEE) for the thermobarometry models are shown with the crosses. The grey bars indicate low velocity zones in a depth of 0–4 km and 9–18 km (Bai & Greenhalgh, 2005).

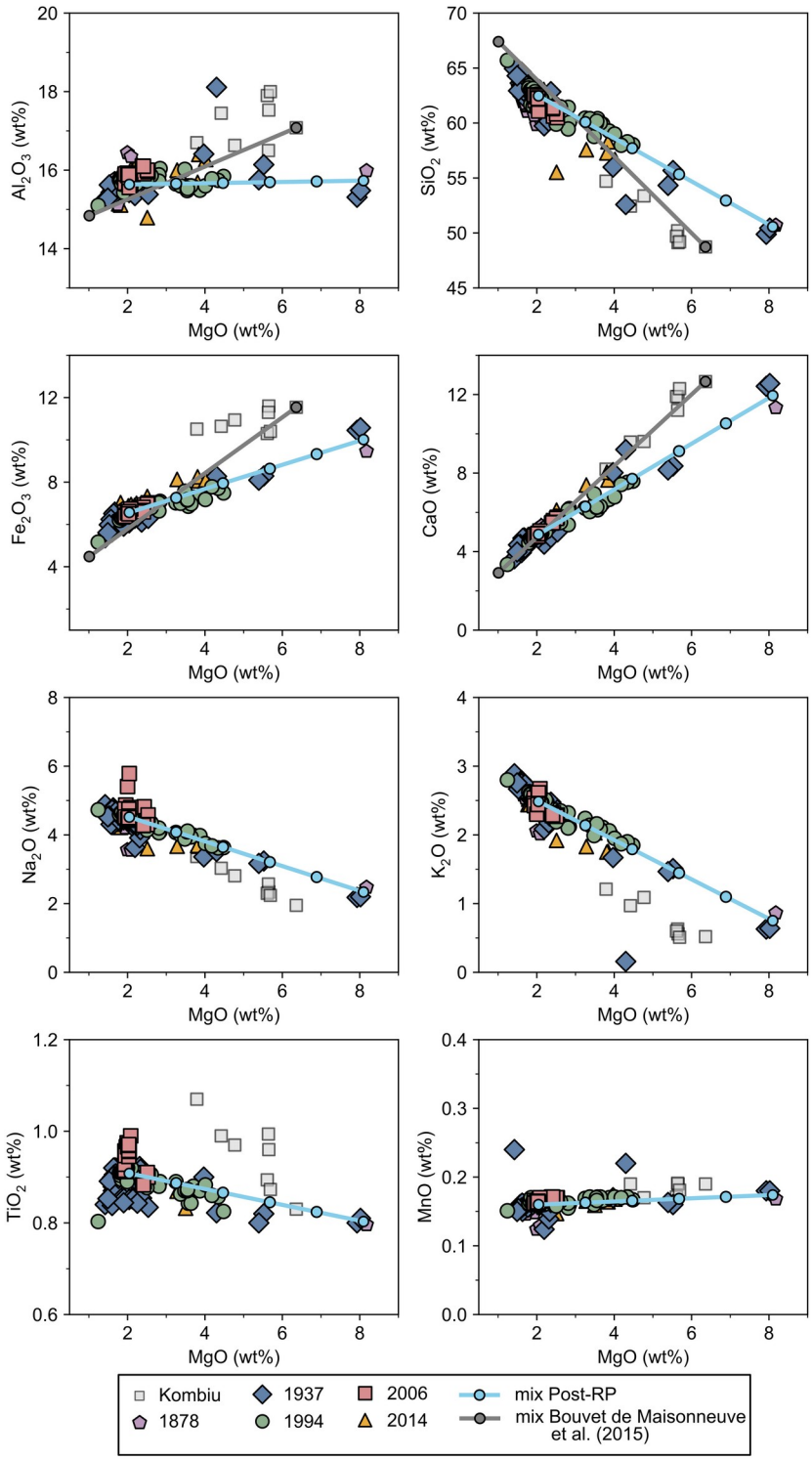


**Figure 15:** Diagrams showing whole-rock compositions for the 1878, 1937, 1994, 2006 and 2014 eruptions of Rabaul and for the Kombiu volcano (literature data from Heming, 1974; Nairn *et al.*, 1989; Patia, 2004; Cunningham *et al.*, 2009; Bouvet de Maisonneuve *et al.*, 2015; Patia *et al.*, 2017; Bernard & Bouvet de Maisonneuve, 2020; Fabbro *et al.*, 2020; Hohl *et al.*, 2022). The light blue line is the mixing line between the average of the most primitive compositions known from the Rabaul eruptions and an average dacitic composition from the Rabaul Pyroclastics (Table 3). The light blue circles on the mixing line show mixing in 20% intervals. The grey line is the mixing line after Bouvet de Maisonneuve *et al.* (2015).

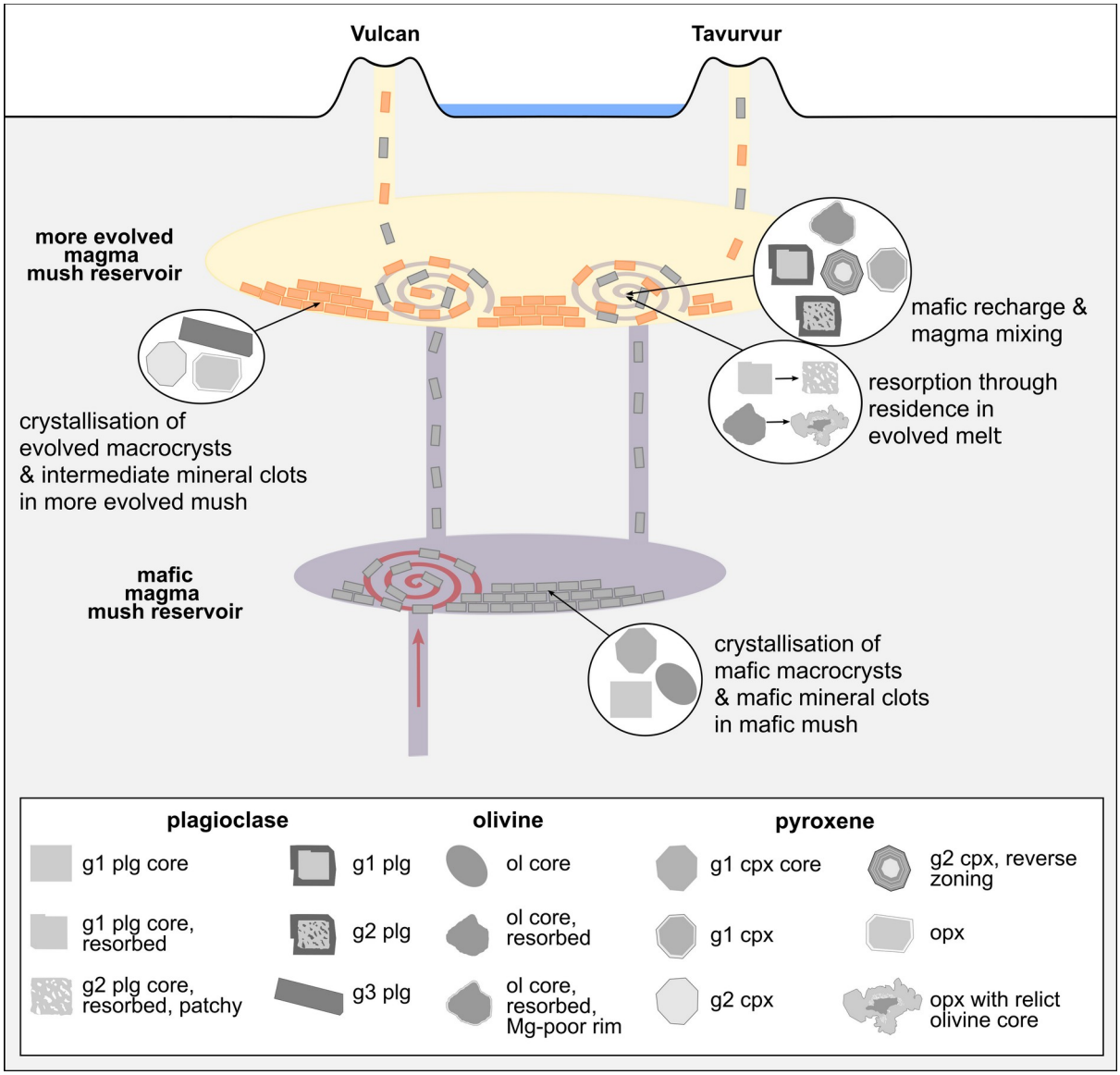


**Figure 16:** Schematic (not to vertical scale) showing where and how the analysed crystal cargo of the 1937, 1994 and 2014 Rabaul eruptions formed and was transferred between magmatic domains. The diagram summarises the two crystal-mush domains resolved by the mineral populations and clot textures of this study, a mafic mush and a more evolved andesitic–dacitic mush, and the transfer of a mafic crystal cargo into the evolved domain during recharge and mixing. The vertical arrangement, with the mafic mush shown deeper, is not constrained by our data, but it follows the deeper of the two seismic low-velocity zones imaged beneath the caldera (Bai & Greenhalgh, 2005; Itikarai, 2008) and the general expectation that more primitive magmas occupy deeper levels in transcrustal systems (Cashman *et al.,* 2017), and is shown schematically for context only. g = group, plg = plagioclase, cpx = clinopyroxene, opx = orthopyroxene.